Journal of Computational Physics

A coupled finite element approach to spatially resolved lithium plating and stripping in three-dimensional anode microstructures of lithium-ion cells
--Manuscript Draft--

Manuscript Number:	
Article Type:	Regular Article
Keywords:	lithium plating; lithium stripping; three-dimensional electrode microstructure; coupled finite element approach; regularization method; Newton-Raphson method
Corresponding Author:	Rui Fang, M.Sc. GERMANY
First Author:	Rui Fang, M.Sc.
Order of Authors:	Rui Fang, M.Sc.
	Christoph Paul Schmidt, M.Sc.
	Wolfgang A. Wall, Prof. Dr.-Ing.
Abstract:	In this article, we present a coupled finite element approach to spatially resolved lithium plating and stripping in three-dimensional anode microstructures of lithium-ion cells. The local film thickness of plated lithium at the anode-electrolyte interface is treated as a primary variable in addition to the lithium concentration and the electric potential inside both electrodes as well as the lithium concentration and the electrochemical potential inside the electrolyte. We take the electric resistance of plated lithium into account when evaluating the Butler-Volmer charge transfer kinetics at the anode-electrolyte interface. The overall system of nonlinear equations resulting from discretization in time and space is solved in a monolithic, implicit fashion by the iterative Newton-Raphson method. To ensure stable and fast convergence especially during the final stages of lithium stripping, we introduce a novel regularization technique characterized by a trigonometrical regularization function for the purpose of discontinuity removal, and we show that our regularization is indeed necessary and effective while being superior to an existing one from the literature in several respects. The linear solver is derived from an advanced, physics-oriented preconditioning and solution technique established in one of our previous publications. In a large number of numerical examples, we thoroughly study two different lithium-ion cells involving up to approximately 2.3 million degrees of freedom. We thereby prove that our modeling and simulation approach is straightforwardly applicable to large and complex problem setups, and that it is capable of capturing lithium plating and stripping during continuous cell cycling without any interruptions in the corresponding simulations. Besides validating our implementation and examining various electrochemical properties of lithium plating and stripping, we also demonstrate that our approach is physically plausible and sensitive to overcharging, fast charging, and low-temperature charging as the three major causes of lithium plating. Unlike existing and widely used approaches based on geometric homogenization via morphological model parameters such as the porosity and the tortuosity, our approach offers the opportunity to detect spatial inhomogeneities in the propagation and distribution of plated lithium within anode microstructures. Accurate and in-depth numerical investigations of lithium plating and stripping are thus enabled as a potent alternative to elaborate and often costly experimental studies.
Suggested Reviewers:	Arnulf Latz, Prof. Dr. Professor, HIU: Helmholtz Institute Ulm arnulf.latz@dlr.de important research in the relevant area (partly serving as the groundwork for the present paper), strong expertise in the modeling and simulation of lithium-ion cells in general
	Wolfgang Bessler, Prof. Dr. rer.nat.habil. Professor, Offenburg University of Applied Sciences: Hochschule Offenburg wolfgang.bessler@hs-offenburg.de

	related research on the modeling and simulation of lithium-ion cells, including lithium plating and stripping
	Jianbo Zhang, Prof. Ph.D. Professor, Tsinghua University jbzhang@tsinghua.edu.cn related research on the modeling and simulation of lithium-ion cells, including lithium plating and stripping (partly of direct relevance to the present paper)

A coupled finite element approach to spatially resolved lithium plating and stripping in three-dimensional anode microstructures of lithium-ion cells

Rui Fang[a,*], Christoph P. Schmidt[a], Wolfgang A. Wall[a]

[a]*Technical University of Munich, Institute for Computational Mechanics, Boltzmannstraße 15, 85748 Garching bei München, Germany*

Significance and novelty of this paper

We present a finite element approach to lithium plating and stripping in three-dimensional anode microstructures of lithium-ion cells. Unlike most existing approaches, we resolve spatial variations in the propagation and distribution of plated lithium without geometric homogenization. Our approach considers the electric resistance of plated lithium and covers overcharging, fast charging, and low-temperature charging as the major causes of lithium plating. The coupled system of discrete, nonlinear equations is solved by a monolithic, implicit Newton–Raphson scheme. Stable and fast convergence is ensured by a novel regularization technique, so that continuous cell cycling can be captured without simulation interruptions even in highly challenging problem setups. We thus enable accurate and in-depth numerical investigations as a potent alternative to experimental studies.

*Corresponding author
   Email address:* `fang@lnm.mw.tum.de` (Rui Fang)

Highlights:

- novel finite element approach can capture lithium plating in 3D anode geometries
- approach can resolve spatial variations in the distribution of plated lithium
- model is sensitive to overcharging, fast charging, and low-temperature charging
- novel regularization scheme improves robustness and efficiency of monolithic solver
- model enables uninterrupted simulations of cell cycling even in challenging setups

A coupled finite element approach to spatially resolved lithium plating and stripping in three-dimensional anode microstructures of lithium-ion cells

Rui Fang[a,*], Christoph P. Schmidt[a], Wolfgang A. Wall[a]

[a]*Technical University of Munich, Institute for Computational Mechanics, Boltzmannstraße 15, 85748 Garching bei München, Germany*

Abstract

In this article, we present a coupled finite element approach to spatially resolved lithium plating and stripping in three-dimensional anode microstructures of lithium-ion cells. The local film thickness of plated lithium at the anode-electrolyte interface is treated as a primary variable in addition to the lithium concentration and the electric potential inside both electrodes as well as the lithium concentration and the electrochemical potential inside the electrolyte. We take the electric resistance of plated lithium into account when evaluating the Butler–Volmer charge transfer kinetics at the anode-electrolyte interface. The overall system of nonlinear equations resulting from discretization in time and space is solved in a monolithic, implicit fashion by the iterative Newton–Raphson method. To ensure stable and fast convergence especially during the final stages of lithium stripping, we introduce a novel regularization technique characterized by a trigonometrical regularization function for the purpose of discontinuity removal, and we show that our regularization is indeed necessary and effective while being superior to an existing one from the literature in several respects. The linear solver is derived from an advanced, physics-oriented preconditioning and solution technique established in one of our previous publications. In a large number of numerical examples, we thoroughly study two different lithium-ion cells involving up to approximately 2.3 million degrees of freedom. We thereby prove that our modeling and simulation approach is straightforwardly applicable to large and complex problem setups, and that it is capable of capturing lithium plating and stripping during continuous cell cycling without any interruptions in the corresponding simulations. Besides validating our implementation and examining various electrochemical properties of lithium plating and stripping, we also demonstrate that our approach is physically plausible and sensitive to overcharging, fast charging, and low-temperature charging as the three major causes of lithium plating. Unlike existing and widely used approaches based on geometric homogenization via morphological model parameters such as the porosity and the tortuosity, our approach offers the opportunity to detect spatial inhomogeneities in the propagation and distribution of plated lithium within anode microstructures. Accurate and in-depth numerical investigations of lithium plating and stripping are thus enabled as a potent alternative to elaborate and often costly experimental studies.

Keywords: lithium plating, lithium stripping, three-dimensional electrode microstructure, coupled finite element approach, regularization method, Newton–Raphson method

1. Introduction

Over the past decades, lithium-ion cells have emerged to play a key role for many applications, such as portable devices, electric and hybrid vehicles, and stationary energy storage systems. Besides other advantages, lithium-ion cells offer high energy densities, i.e., large discharge capacities at small sizes and weights [1]. Despite being well-established, lithium-ion cells are still prone to environmental and operational hazards resulting in impaired performance, in reduced lifetime, cyclability, or safety, or even in complete

---

*Corresponding author
Email address: `fang@lnm.mw.tum.de` (Rui Fang)

destruction through effects like thermal runaway [2]. Inner short circuits constitute one of the major challenges not yet resolved and are most often caused by lithium plating and subsequent dendrite formation, i.e., the deposition and growth of metallic lithium on anode surfaces due to reduced intercalation under certain operating conditions [3–5]. Lithium plating can, at least partly, be reverted through lithium stripping, i.e., the consumption of already plated lithium as a consequence of lithium intercalation into the anode or lithium dissolution into the electrolyte [6, 7].

A wide range of in-situ and ex-situ methods have been proposed in the literature to experimentally investigate lithium plating, understand its mechanisms, and identify mitigation strategies. However, the experimental detection of lithium plating occurs either indirectly during cycling via aging effects [8–11] or discharge characteristics [12], or it requires expensive, time-consuming, and complex machinery not readily accessible to most of the research community, including scanning electron microscopes [13–16], optical microscopes [17–19], nuclear magnetic resonance spectrometers [15, 20], electron paramagnetic resonance spectrometers [21], and neutron diffraction facilities [22]. Therefore, theoretical considerations combined with numerical simulations become more and more important, since they often grant valuable insights for comparatively little effort [23].

Almost all published modeling and simulation approaches to lithium plating and stripping [7, 24–30] build on the one-dimensional porous electrode theory established in [31, 32] or on equivalent circuit theory. Despite being widely used, these theories are seldom very accurate, comprehensive and predictive due to a number of simplifications. Most importantly, three-dimensional cell microstructures are geometrically homogenized via morphological model parameters such as porosity and tortuosity. This leads to a reduced computational complexity on the one hand, but also to an inherent neglect of microstructural inhomogeneities on the other hand. As a consequence, lithium plating and stripping are not spatially resolved and three-dimensional, local effects are not captured, e.g., self-accelerated lithium plating induced by changes of electrochemical properties in the vicinity of already deposited lithium films in large pouch cells [14]. Models resolving the nucleation and growth of dendrites have been presented, but are restricted to single anode particles or dendrites [33–35]. Furthermore, most of the current contributions in the literature exclusively consider lithium plating and ignore lithium stripping [25, 36]. In cases where lithium stripping does come into focus, it is usually treated separately and not combined with lithium plating in one single simulation [6]. The investigation of electrochemical interactions between lithium plating and stripping is thus prevented. Additional simplifying assumptions include the reduction of full cells to half cells without cathode microstructures [37], the disregard of the electric resistance of deposited lithium films [6] and the usage of the Tafel law instead of the more general Butler–Volmer charge transfer kinetics to describe lithium plating and stripping [25]. And lastly, to the best of our knowledge, no single publication examines all three major causes of lithium plating, i.e., overcharging, fast charging, and low-temperature charging.

In this article, we introduce a comprehensive modeling and simulation approach to spatially resolved lithium plating and stripping in anode microstructures to address all of the aforementioned issues. In particular, our approach can, for the first time, be consistently incorporated into finite element simulations of three-dimensional lithium-ion cells without geometric homogenization and with only a minimum of simplifications. Such three-dimensional simulations have recently been promoted by significant progresses in computational power, numerical methods, and tomography techniques for lithium-ion cells. Another novelty of our approach is that it is capable of capturing lithium plating and stripping during one single simulation without any interruptions, so that the cycling behavior of lithium-ion cells in the presence of lithium plating and stripping can be thoroughly studied. The electric resistance of plated lithium is taken into account by our approach via a corresponding term subtracted from the plain Butler–Volmer overpotential. Beyond that, all three major reasons for lithium plating are covered by our approach, as we will demonstrate in our numerical examples. Although we restrict ourselves to lithium-ion cells with liquid electrolytes in our present contribution, our work may also be relevant to comparable electrochemical systems exhibiting lithium plating and stripping, e.g., to all-solid-state lithium-ion cells.

More technically speaking, we developed a coupled framework to enrich a basic, standard finite element model for lithium-ion cells by additional functionality for lithium plating and stripping. The local film thickness of plated lithium is introduced as a primary variable and iteratively computed via the Newton–
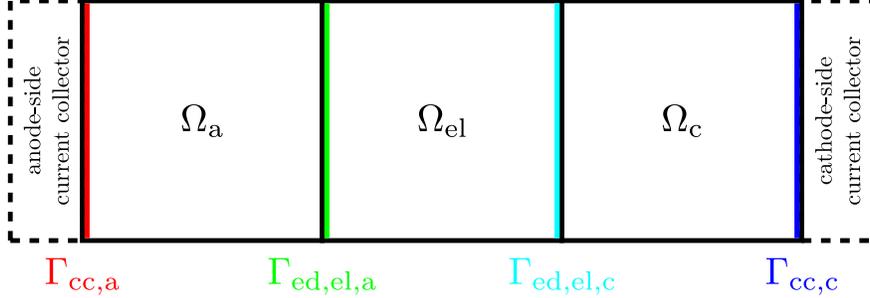
Figure 1: Schematic setup of computational domain.

Raphson method as the nonlinear solver. We exclusively consider a monolithic, implicit solution algorithm in this work, since partitioned variants are often less robust and efficient in many fields of application, including lithium-ion cell modeling [38, 39], thermo-structure interaction [40], and especially fluid-structure interaction [41, 42]. To ensure stable and fast convergence of the Newton–Raphson method, we designed and implemented a novel regularization technique, and we show that our technique has advantages as compared to an existing one in the finite volume framework from [6, 37, 43] in that it is physically more justified and computationally less intrusive while still yielding good convergence of the Newton–Raphson method even during the most critical and challenging simulation phases. These are identified as the time periods around initial occurrences of lithium plating, around final stages of lithium stripping when plated lithium is completely consumed, and around reversals of the overall electric current from charge to discharge and vice versa during cycling.

We structured the remainder of this work as follows: Section 2 defines our modeling and simulation approach, including all underlying governing equations and details on their numerical treatment. Special attention is drawn to the anode-electrolyte interface, where lithium plating and stripping need to be captured. In Section 3, we elaborate on our novel regularization technique and compare it to the one originally proposed in [6]. Selected numerical examples are presented and discussed in Section 4, where we exclusively examine three-dimensional problem setups involving either academic or realistic electrode microstructures and up to approximately 2.3 million degrees of freedom. Both the influence of operating conditions on lithium plating and stripping and, in turn, the influence of lithium plating and stripping on charge and discharge characteristics are thoroughly studied. The findings demonstrate that our approach is sensitive to all three major causes of lithium plating mentioned before, and that it delivers physically reasonable results in each case. Finally, Section 5 summarizes our work and gives an outlook on potential ideas for future research.

2. Problem definition

We consider a three-dimensional, isothermal lithium-ion cell during the time interval $t \in [0; t^{\mathrm{end}}]$. The electrolyte contains a binary salt dissociated into equally many positive lithium ions and negative counterions. The cell is mathematically represented by a non-empty, connected, open set $\Omega \in \mathbb{R}^3$ and bounded by a sufficiently smooth outer surface $\partial\Omega$, as conceptually illustrated in Figure 1. The anode phase Ω_{a} and the cathode phase Ω_{c} constitute the electrode phase $\Omega_{\mathrm{ed}} = \Omega_{\mathrm{a}} \cup \Omega_{\mathrm{c}}$ bounded by $\partial\Omega_{\mathrm{ed}}$. The electrolyte phase is denoted by Ω_{el} and bounded by $\partial\Omega_{\mathrm{el}}$. The anode-side and cathode-side electrode-electrolyte interfaces are symbolized by $\Gamma_{\mathrm{ed,el,a}} = \partial\Omega_{\mathrm{a}} \setminus \partial\Omega$ and $\Gamma_{\mathrm{ed,el,c}} = \partial\Omega_{\mathrm{c}} \setminus \partial\Omega$, respectively. The contact surfaces between the electrodes and the corresponding current collectors are indicated by $\Gamma_{\mathrm{cc,a}}$ on the anode side and by $\Gamma_{\mathrm{cc,c}}$ on the cathode side. No further entities are part of the present model.

In the subsequent sections, we give a brief overview of the conservation equations and associated interface, boundary, and initial conditions implemented in our model. We also comment on time and space discretization as well as on constraint enforcement strategies. As a result, we obtain a finite element formulation involving a discrete system of nonlinear equations to be linearized and iteratively solved according to the Newton–Raphson method.

3

2.1. Conservation equations

The lithium-ion cell from Figure 1 is assumed to obey a set of two conservation equations for lithium mass and electric charge, so that the primary variables are given by the lithium concentration and the electric or electrochemical potential. Conservation of lithium mass inside the electrode and electrolyte phases, labeled by the respective indices $(\cdot)_{\mathrm{ed}}$ and $(\cdot)_{\mathrm{el}}$, is expressed as

$$\frac{\partial c_{\mathrm{ed/el}}}{\partial t} + \nabla \cdot \boldsymbol{j}_{\mathrm{ed/el}} = 0 \qquad \text{in } \Omega_{\mathrm{ed/el}} \times (0, t^{\mathrm{end}}), \tag{1}$$

where c_{ed} and c_{el} are lithium concentrations, and $\boldsymbol{j}_{\mathrm{ed}}$ and $\boldsymbol{j}_{\mathrm{el}}$ are lithium mass flux densities according to

$$\boldsymbol{j}_{\mathrm{ed}} = -D_{\mathrm{ed}} \nabla c_{\mathrm{ed}}, \qquad \boldsymbol{j}_{\mathrm{el}} = -D_{\mathrm{el}} \nabla c_{\mathrm{el}} + \frac{t_{\mathrm{el}}}{F} \boldsymbol{i}_{\mathrm{el}}. \tag{2}$$

Herein, D_{ed} and D_{el} stand for diffusion coefficients of lithium, t_{el} denotes the lithium-ion transference number, and F indicates the Faraday constant. The electric current densities $\boldsymbol{i}_{\mathrm{ed}}$ and $\boldsymbol{i}_{\mathrm{el}}$ inside the electrode and electrolyte phases are written as

$$\boldsymbol{i}_{\mathrm{ed}} = -\sigma_{\mathrm{ed}} \nabla \Phi_{\mathrm{ed}}, \qquad \boldsymbol{i}_{\mathrm{el}} = -\kappa_{\mathrm{el}} \nabla \Phi_{\mathrm{el}} + \frac{2RT\kappa_{\mathrm{el}}}{F} \left(1 + \frac{\partial \ln f_{\mathrm{el}}}{\partial \ln c_{\mathrm{el}}}\right) (1 - t_{\mathrm{el}}) \nabla \ln c_{\mathrm{el}}, \tag{3}$$

where σ_{ed} and Φ_{ed} are the electronic conductivity and the electric potential inside the electrode phase, and κ_{el}, Φ_{el}, and f_{el} are the ionic conductivity, the electrochemical potential, and the mean activity coefficient inside the electrolyte phase [32]. The gas constant and the temperature are symbolized by R and T, respectively. The following expression from [44] is adopted for κ_{el}:

$$\kappa_{\mathrm{el}} = A_{\mathrm{el}} c_{\mathrm{el}} \exp\left(k_{\mathrm{el}} c_{\mathrm{el}}^{d_{\mathrm{el}}}\right). \tag{4}$$

Herein, A_{el}, k_{el}, and d_{el} are fitted model parameters. We remark that the literature offers different methods of model parameter determination based on electrochemical experiments, see, e.g., our previous work presented in [45–47].

In addition to lithium mass, electric charge is also conserved inside the electrode and electrolyte phases:

$$\nabla \cdot \frac{\boldsymbol{i}_{\mathrm{ed/el}}}{F} = 0 \qquad \text{in } \Omega_{\mathrm{ed/el}} \times [0, t^{\mathrm{end}}]. \tag{5}$$

The scaling by $\frac{1}{F}$ is introduced to transform $\boldsymbol{i}_{\mathrm{ed}}$ and $\boldsymbol{i}_{\mathrm{el}}$ to the same order of magnitude as $\boldsymbol{j}_{\mathrm{ed}}$ and $\boldsymbol{j}_{\mathrm{el}}$.

2.2. Interface conditions

We now focus on the electrolyte side of the anode-electrolyte interface $\Gamma_{\mathrm{ed,el,a}}$ from Figure 1, where the total electric current density in normal direction is given by

$$i_{\mathrm{ed,el}} = i_{\mathrm{ed,el}}^{\mathrm{int}} + i_{\mathrm{ed,el}}^{\mathrm{pl}}. \tag{6}$$

The first summand is termed "intercalation current" and captures lithium intercalation and deintercalation, while we refer to the second one as "plating current" governing lithium plating and stripping. Both currents are modeled by the classical Butler–Volmer charge transfer kinetics [32]. The intercalation current can thus be written as

$$i_{\mathrm{ed,el}}^{\mathrm{int}} = i_0^{\mathrm{int}} \left(\exp\left(\frac{\alpha_{\mathrm{a}}^{\mathrm{int}} F \eta^{\mathrm{int}}}{RT}\right) - \exp\left(-\frac{\alpha_{\mathrm{c}}^{\mathrm{int}} F \eta^{\mathrm{int}}}{RT}\right)\right), \tag{7}$$

where i_0^{int} denotes the interfacial exchange current density, $\alpha_{\mathrm{a}}^{\mathrm{int}}$ and $\alpha_{\mathrm{c}}^{\mathrm{int}}$ stand for the anodic and cathodic transfer coefficients, and η^{int} is the interfacial overpotential. We have

$$i_0^{\mathrm{int}} = k^{\mathrm{int}} F c_{\mathrm{ed}}^{\alpha_{\mathrm{c}}^{\mathrm{int}}} (c_{\mathrm{ed,max}} - c_{\mathrm{ed}})^{\alpha_{\mathrm{a}}^{\mathrm{int}}} c_{\mathrm{el}}^{\alpha_{\mathrm{a}}^{\mathrm{int}}}, \tag{8}$$

4

where k^{int} is the rate constant of the interfacial charge transfer reaction and $c_{\mathrm{ed,max}}$ is the maximum saturation concentration of intercalated lithium inside the anode, and

$$\eta^{\mathrm{int}} = \Phi_{\mathrm{ed}} - \Phi_{\mathrm{el}} - \Phi_0^{\mathrm{int}} - \frac{d_{\mathrm{Li}} i_{\mathrm{ed,el}}^{\mathrm{int}}}{\sigma_{\mathrm{Li}}}, \tag{9}$$

where Φ_0^{int} is the open-circuit equilibrium potential inside the anode, d_{Li} is the local film thickness of plated lithium, and σ_{Li} is the electronic conductivity of lithium. The last part of the interfacial overpotential stems from the electric resistance of plated lithium, and we adopt the semi-empirical Redlich–Kister expansion [48] for Φ_0^{int}:

$$\Phi_0^{\mathrm{int}} = \frac{\Delta G}{F} + \frac{RT}{F} \ln\left(\frac{1 - X_{\mathrm{ed}}}{X_{\mathrm{ed}}}\right) + \sum_m \frac{A_m}{F}\left((2X_{\mathrm{ed}} - 1)^{m+1} - \frac{2mX_{\mathrm{ed}}\left(1 - X_{\mathrm{ed}}\right)}{(2X_{\mathrm{ed}} - 1)^{1-m}}\right). \tag{10}$$

Herein, the change in the Gibbs free energy during interfacial charge transfer is given by ΔG, the polynomial Redlich–Kister coefficients for $m = 0, 1, 2, \ldots$ are denoted by A_m, and the local mole fraction of intercalated lithium inside the anode is defined as

$$X_{\mathrm{ed}} = \frac{c_{\mathrm{ed}}}{c_{\mathrm{ed,max}}}. \tag{11}$$

Besides the intercalation current, the plating current also obeys the Butler–Volmer charge transfer kinetics, albeit in a modified form:

$$i_{\mathrm{ed,el}}^{\mathrm{pl}} = \begin{cases} i_0^{\mathrm{pl}}\left(\exp\left(\frac{\alpha_{\mathrm{a}}^{\mathrm{pl}} F \eta^{\mathrm{pl}}}{RT}\right) - \exp\left(-\frac{\alpha_{\mathrm{c}}^{\mathrm{pl}} F \eta^{\mathrm{pl}}}{RT}\right)\right) & \text{if } \eta^{\mathrm{pl}} < 0 \text{ or } d_{\mathrm{Li}} > 0 \\ 0 & \text{otherwise} \end{cases}, \tag{12}$$

$$i_0^{\mathrm{pl}} = k^{\mathrm{pl}} F c_{\mathrm{el}}^{\alpha_{\mathrm{a}}^{\mathrm{pl}}}, \tag{13}$$

$$\eta^{\mathrm{pl}} = \Phi_{\mathrm{ed}} - \Phi_{\mathrm{el}} - \underbrace{\Phi_0^{\mathrm{pl}}}_{=0} - \frac{d_{\mathrm{Li}} i_{\mathrm{ed,el}}^{\mathrm{pl}}}{\sigma_{\mathrm{Li}}}. \tag{14}$$

The quantities i_0^{pl}, $\alpha_{\mathrm{a}}^{\mathrm{pl}}$, $\alpha_{\mathrm{c}}^{\mathrm{pl}}$, η^{pl}, k^{pl}, and Φ_0^{pl} herein are completely analogous to their respective counterparts characterizing the intercalation current. However, we notice three differences in the corresponding equations: Firstly, the plating current is only non-zero if the so-called plating condition is fulfilled, i.e., if the occurrence of lithium plating is thermodynamically favorable to pure lithium intercalation in the case of $\eta^{\mathrm{pl}} < 0$ according to the thermodynamically consistent derivation in [6], or otherwise if lithium stripping is possible due to an already deposited lithium film with $d_{\mathrm{Li}} > 0$. Secondly, the interfacial exchange current density does not penetrate the anode surface and thus does not depend on the interfacial lithium concentration inside the anode. And lastly, the open-circuit equilibrium potential as part of the interfacial overpotential vanishes with respect to plated lithium by definition.

Conservation of lithium mass and electric charge at the anode-electrolyte interface determines the temporal evolution of the local film thickness of plated lithium according to

$$\frac{\partial d_{\mathrm{Li}}}{\partial t} + \frac{M_{\mathrm{Li}} i_{\mathrm{ed,el}}^{\mathrm{pl}}}{\rho_{\mathrm{Li}} \sigma_{\mathrm{Li}} F} = 0 \qquad \text{on } \Gamma_{\mathrm{ed,el,a}} \times (0, t^{\mathrm{end}}), \tag{15}$$

where M_{Li} and ρ_{Li} denote the molar mass and density of lithium, respectively. It also follows that

$$\boldsymbol{j}_{\mathrm{ed}} \cdot \boldsymbol{n}_{\mathrm{ed,el}} = \frac{1}{F} \boldsymbol{i}_{\mathrm{ed}} \cdot \boldsymbol{n}_{\mathrm{ed,el}} = \frac{1}{F} i_{\mathrm{ed,el}}^{\mathrm{int}} \qquad \text{on } \Gamma_{\mathrm{ed,el,a}} \times [0, t^{\mathrm{end}}], \tag{16}$$

$$\boldsymbol{j}_{\mathrm{el}} \cdot \boldsymbol{n}_{\mathrm{ed,el}} = \frac{1}{F} \boldsymbol{i}_{\mathrm{el}} \cdot \boldsymbol{n}_{\mathrm{ed,el}} = \frac{1}{F}\left(i_{\mathrm{ed,el}}^{\mathrm{int}} + i_{\mathrm{ed,el}}^{\mathrm{pl}}\right) = \frac{1}{F} i_{\mathrm{ed,el}} \qquad \text{on } \Gamma_{\mathrm{ed,el,a}} \times [0, t^{\mathrm{end}}], \tag{17}$$

where $\boldsymbol{n}_{\mathrm{ed,el}}$ is the interfacial unit normal vector pointing from the anode side to the electrolyte side.

The interface conditions (16) and (17) as well as the underlying equations (6) through (11) analogously hold for the cathode-electrolyte interface $\Gamma_{\mathrm{ed,el,c}}$ from Figure 1 after dropping all contributions related to lithium plating and stripping, i.e., after setting $i_{\mathrm{ed,el}}^{\mathrm{pl}} = d_{\mathrm{Li}} = 0$. For the sake of brevity, we do not explicitly write out all equations once again.

A proper treatment of the interface conditions (15–17) is numerically challenging for two reasons: Firstly, the interface conditions involve the highly nonlinear Butler–Volmer charge transfer kinetics (7) and (12). The latter governing the plating current is even discontinuous, as will be further examined in Section 3. And secondly, the interface conditions induce a strong electrochemical interaction between the electrode and electrolyte phases, since they not only incorporate all primary variables, but also have an impact on all conservation equations (1) and (5). Due to this nonlinear and strong coupling, we do not consider the electrode and electrolyte phases separately, but rather establish a single, unified system of equations capturing both phases, see Section 2.5.

2.3. Boundary conditions and initial conditions

We assume that the anode-side and cathode-side current collectors of the lithium-ion cell from Figure 1 are impermeable to lithium, and that the entire cell is symmetric in lateral direction. Accordingly, we formulate the homogeneous Neumann boundary conditions

$$-\boldsymbol{j}_{\mathrm{ed/el}} \cdot \boldsymbol{n} = 0 \qquad \text{on } \partial\Omega_{\mathrm{ed/el}} \cap \partial\Omega \times [0, t^{\mathrm{end}}], \tag{18}$$

$$-\boldsymbol{i}_{\mathrm{ed}} \cdot \boldsymbol{n} = 0 \qquad \text{on } \partial\Omega_{\mathrm{ed}} \setminus (\Gamma_{\mathrm{cc,a}} \cup \Gamma_{\mathrm{cc,c}} \cup \Gamma_{\mathrm{ed,el}}) \times [0, t^{\mathrm{end}}], \tag{19}$$

$$-\boldsymbol{i}_{\mathrm{el}} \cdot \boldsymbol{n} = 0 \qquad \text{on } \partial\Omega_{\mathrm{el}} \setminus \Gamma_{\mathrm{ed,el}} \times [0, t^{\mathrm{end}}], \tag{20}$$

where $\boldsymbol{n}$ denotes the outward-pointing unit normal vector, and $\Gamma_{\mathrm{ed,el}} = \Gamma_{\mathrm{ed,el,a}} \cup \Gamma_{\mathrm{ed,el,c}}$. Furthermore, we introduce a homogeneous Dirichlet boundary condition to set the electric potential inside the anode to a reference value of zero at the anode-side current collector:

$$\Phi_{\mathrm{ed}} = 0 \qquad \text{on } \Gamma_{\mathrm{cc,a}} \times [0, t^{\mathrm{end}}]. \tag{21}$$

At the cathode-side current collector, we impose a Neumann boundary condition involving a normal electric current density $\hat{i}_{\mathrm{ed}}$:

$$-\boldsymbol{i}_{\mathrm{ed}} \cdot \boldsymbol{n} = \hat{i}_{\mathrm{ed}} \qquad \text{on } \Gamma_{\mathrm{cc,c}} \times [0, t^{\mathrm{end}}]. \tag{22}$$

The value of $\hat{i}_{\mathrm{ed}}$ is positive during charging, zero during relaxation, and negative during discharging. The magnitude of $\hat{i}_{\mathrm{ed}}$ is directly correlated with the so-called C-rate, defined via the state of charge of the cell or, equivalently, the state of charge of the limiting electrode with the smaller capacity:

$$\mathrm{SOC} = \frac{\frac{1}{V_{\mathrm{ed}}} \int_{V_{\mathrm{ed}}} c_{\mathrm{ed}} \, \mathrm{d}V_{\mathrm{ed}} - c_{\mathrm{ed}}^{0\%}}{c_{\mathrm{ed}}^{100\%} - c_{\mathrm{ed}}^{0\%}}. \tag{23}$$

Herein, the volume of the limiting electrode is given by V_{ed}, while $c_{\mathrm{ed}}^{0\%}$ and $c_{\mathrm{ed}}^{100\%}$ stand for the average lithium concentrations inside the limiting electrode at 0% and 100% state of charge, respectively. A C-rate of $x\,\mathrm{C}$ changes the state of charge of the cell from 0% to 100% or vice versa within $\frac{1}{x}$ hours under the assumption of galvanostatic operation. Controlling the sign and magnitude of $\hat{i}_{\mathrm{ed}}$ thus allows us to capture specific cell cycling protocols without any interruptions in the corresponding simulations.

Initially, the cell is assumed to be in static equilibrium without any plated lithium according to the initial conditions

$$c_{\mathrm{ed/el}} = c_{\mathrm{ed/el}}^{0} = \mathrm{const.} \qquad \text{in } \Omega_{\mathrm{ed/el}} \times \{0\}, \tag{24}$$

$$d_{\mathrm{Li}} = 0 \qquad \text{on } \Gamma_{\mathrm{ed,el,a}} \times \{0\}. \tag{25}$$

Since the conservation equations (5) for electric charge are stationary, we do not prescribe the initial electric and electrochemical potential fields Φ_{ed}^{0} and Φ_{el}^{0} directly. Instead, we consistently construct them from the conservation equations (5), the interface conditions (16) and (17), the boundary conditions (19–22), and the initial conditions (24) and (25).

2.4. Discretization in time and space

For the purpose of time discretization, we split the time period of interest into contiguous, non-overlapping, not necessarily uniform time intervals Δt. The n-th interval starts at the time t^{n-1} and ends at the time t^n. The transient conservation equations (1) for lithium mass as well as the transient evolution equation (15) for the local film thickness of plated lithium are discretized by the second-order accurate Crank–Nicolson time integration scheme, while the stationary conservation equations (5) for electric charge are solved at the end time t^n of each interval. As a result, we obtain a fully coupled and implicit system of equations, where the local film thickness constitutes a primary variable in addition to the lithium concentrations and the electric or electrochemical potentials inside the electrode and electrolyte phases. All primary variables are evaluated simultaneously, so that lithium plating and stripping are consistently incorporated into our model.

After time discretization, space discretization is performed according to the well-known Bubnov–Galerkin finite element method combined with isoparametric interpolation, see, e.g., [49, 50] for details. The interface conditions (16) and (17) can be straightforwardly inserted into the respective interface integrals in the weak formulation of the semi-discrete conservation equations (1) and (5). However, the intercalation and plating currents appearing in both interface conditions are only implicitly given by the Butler–Volmer charge transfer kinetics (7) and (12), since the interfacial overpotentials (9) and (14) contained therein in turn depend on the intercalation and plating currents, respectively. We thus apply the iterative Newton–Raphson method as a local root-finding algorithm to determine the intercalation and plating currents at each spatial integration point. Furthermore, we choose conforming finite element meshes with pairwise coinciding nodes at the anode-electrolyte and cathode-electrolyte interfaces to obtain an inherently consistent interface coupling, i.e., an exact satisfaction of both interface conditions (16) and (17) in a weak sense. A generalization towards non-conforming finite element meshes can be established with little additional effort following the mortar-based space discretization technique introduced in [51]. We remark that each numerical example from Section 4 involves a three-dimensional computational domain discretized by tetrahedral finite elements with first-order Lagrange polynomials as shape functions.

2.5. Monolithic system of linear equations

After discretization in time and space, we arrive at a discrete system of nonlinear equations to be solved for each time interval. The local film thickness of plated lithium is consistently and implicitly integrated into the system as follows:

$$\begin{pmatrix} \mathbf{R}_{c_{\mathrm{ed}}}\left(\mathbf{c}_{\mathrm{ed}}, \boldsymbol{\Phi}_{\mathrm{ed}}, \mathbf{c}_{\mathrm{el}}, \boldsymbol{\Phi}_{\mathrm{el}}, \mathbf{d}_{\mathrm{Li}}\right) \\ \mathbf{R}_{\Phi_{\mathrm{ed}}}\left(\mathbf{c}_{\mathrm{ed}}, \boldsymbol{\Phi}_{\mathrm{ed}}, \mathbf{c}_{\mathrm{el}}, \boldsymbol{\Phi}_{\mathrm{el}}, \mathbf{d}_{\mathrm{Li}}\right) \\ \mathbf{R}_{c_{\mathrm{el}}}\left(\mathbf{c}_{\mathrm{ed}}, \boldsymbol{\Phi}_{\mathrm{ed}}, \mathbf{c}_{\mathrm{el}}, \boldsymbol{\Phi}_{\mathrm{el}}, \mathbf{d}_{\mathrm{Li}}\right) \\ \mathbf{R}_{\Phi_{\mathrm{el}}}\left(\mathbf{c}_{\mathrm{ed}}, \boldsymbol{\Phi}_{\mathrm{ed}}, \mathbf{c}_{\mathrm{el}}, \boldsymbol{\Phi}_{\mathrm{el}}, \mathbf{d}_{\mathrm{Li}}\right) \\ \mathbf{R}_{d_{\mathrm{Li}}}\left(\boldsymbol{\Phi}_{\mathrm{ed}}, \mathbf{c}_{\mathrm{el}}, \boldsymbol{\Phi}_{\mathrm{el}}, \mathbf{d}_{\mathrm{Li}}\right) \end{pmatrix} = \begin{pmatrix} \mathbf{0} \\ \mathbf{0} \\ \mathbf{0} \\ \mathbf{0} \\ \mathbf{0} \end{pmatrix}. \tag{26}$$

Herein, $\mathbf{R}_{(\cdot)}$ denotes the discrete residual vector corresponding to the primary variable in the subscript, i.e., to one of the governing equations (1), (5), and (15). The discrete solution vectors $\mathbf{c}_{\mathrm{ed/el}}$, $\boldsymbol{\Phi}_{\mathrm{ed/el}}$, and $\mathbf{d}_{\mathrm{Li}}$ indicated as arguments contain the respective nodal degrees of freedom at the time t^n, i.e., the lithium concentration and electric or electrochemical potential values inside the electrode and electrolyte phases, as well as the local film thickness values at the anode-electrolyte interface. The total number of rows in the system naturally equals the total number of degrees of freedom resulting from the discretization. We point out that $\mathbf{R}_{d_{\mathrm{Li}}}$ does not depend on $\mathbf{c}_{\mathrm{ed}}$, given that the associated governing equation (15) does not involve c_{ed}.

Since most of the governing equations underlying the system are strongly coupled and nonlinear, we adopt the iterative Newton–Raphson method as the global solution scheme. To this end, we establish a monolithic, sparse system of linear equations containing consistent linearizations of all discrete residual vectors with

7

respect to all discrete solution vectors:

$$
\begin{pmatrix}
\frac{\partial \mathbf{R}_{c_{\mathrm{ed}}}}{\partial \mathbf{c}_{\mathrm{ed}}} & \frac{\partial \mathbf{R}_{c_{\mathrm{ed}}}}{\partial \boldsymbol{\Phi}_{\mathrm{ed}}} & \frac{\partial \mathbf{R}_{c_{\mathrm{ed}}}}{\partial \mathbf{c}_{\mathrm{el}}} & \frac{\partial \mathbf{R}_{c_{\mathrm{ed}}}}{\partial \boldsymbol{\Phi}_{\mathrm{el}}} & \frac{\partial \mathbf{R}_{c_{\mathrm{ed}}}}{\partial \mathbf{d}_{\mathrm{Li}}} \\[6pt]
\frac{\partial \mathbf{R}_{\Phi_{\mathrm{ed}}}}{\partial \mathbf{c}_{\mathrm{ed}}} & \frac{\partial \mathbf{R}_{\Phi_{\mathrm{ed}}}}{\partial \boldsymbol{\Phi}_{\mathrm{ed}}} & \frac{\partial \mathbf{R}_{\Phi_{\mathrm{ed}}}}{\partial \mathbf{c}_{\mathrm{el}}} & \frac{\partial \mathbf{R}_{\Phi_{\mathrm{ed}}}}{\partial \boldsymbol{\Phi}_{\mathrm{el}}} & \frac{\partial \mathbf{R}_{\Phi_{\mathrm{ed}}}}{\partial \mathbf{d}_{\mathrm{Li}}} \\[6pt]
\frac{\partial \mathbf{R}_{c_{\mathrm{el}}}}{\partial \mathbf{c}_{\mathrm{ed}}} & \frac{\partial \mathbf{R}_{c_{\mathrm{el}}}}{\partial \boldsymbol{\Phi}_{\mathrm{ed}}} & \frac{\partial \mathbf{R}_{c_{\mathrm{el}}}}{\partial \mathbf{c}_{\mathrm{el}}} & \frac{\partial \mathbf{R}_{c_{\mathrm{el}}}}{\partial \boldsymbol{\Phi}_{\mathrm{el}}} & \frac{\partial \mathbf{R}_{c_{\mathrm{el}}}}{\partial \mathbf{d}_{\mathrm{Li}}} \\[6pt]
\frac{\partial \mathbf{R}_{\Phi_{\mathrm{el}}}}{\partial \mathbf{c}_{\mathrm{ed}}} & \frac{\partial \mathbf{R}_{\Phi_{\mathrm{el}}}}{\partial \boldsymbol{\Phi}_{\mathrm{ed}}} & \frac{\partial \mathbf{R}_{\Phi_{\mathrm{el}}}}{\partial \mathbf{c}_{\mathrm{el}}} & \frac{\partial \mathbf{R}_{\Phi_{\mathrm{el}}}}{\partial \boldsymbol{\Phi}_{\mathrm{el}}} & \frac{\partial \mathbf{R}_{\Phi_{\mathrm{el}}}}{\partial \mathbf{d}_{\mathrm{Li}}} \\[6pt]
\mathbf{0} & \frac{\partial \mathbf{R}_{d_{\mathrm{Li}}}}{\partial \boldsymbol{\Phi}_{\mathrm{ed}}} & \frac{\partial \mathbf{R}_{d_{\mathrm{Li}}}}{\partial \mathbf{c}_{\mathrm{el}}} & \frac{\partial \mathbf{R}_{d_{\mathrm{Li}}}}{\partial \boldsymbol{\Phi}_{\mathrm{el}}} & \frac{\partial \mathbf{R}_{d_{\mathrm{Li}}}}{\partial \mathbf{d}_{\mathrm{Li}}}
\end{pmatrix}\Bigg|_{\ell}
\cdot
\begin{pmatrix}
\Delta \mathbf{c}_{\mathrm{ed}} \\[6pt]
\Delta \boldsymbol{\Phi}_{\mathrm{ed}} \\[6pt]
\Delta \mathbf{c}_{\mathrm{el}} \\[6pt]
\Delta \boldsymbol{\Phi}_{\mathrm{el}} \\[6pt]
\Delta \mathbf{d}_{\mathrm{Li}}
\end{pmatrix}\Bigg|_{\ell}
= -
\begin{pmatrix}
\mathbf{R}_{c_{\mathrm{ed}}} \\[6pt]
\mathbf{R}_{\Phi_{\mathrm{ed}}} \\[6pt]
\mathbf{R}_{c_{\mathrm{el}}} \\[6pt]
\mathbf{R}_{\Phi_{\mathrm{el}}} \\[6pt]
\mathbf{R}_{d_{\mathrm{Li}}}
\end{pmatrix}\Bigg|_{\ell} .
\tag{27}
$$

The discrete solution increment vectors $\Delta(\cdot)$ to be solved for in each Newton–Raphson iteration step ℓ are iteratively added to the respective discrete solution vectors until convergence is achieved according to a predefined criterion. In all numerical examples presented in Section 4, we consider the Newton–Raphson method to be converged once the relative L^2 norms of the discrete solution increment vectors pertaining to the overall lithium concentration field and electric or electrochemical potential field inside the entire cell have both fallen below a convergence tolerance of 10^{-10}. Since $\mathbf{R}_{d_{\mathrm{Li}}}$ is independent of $\mathbf{c}_{\mathrm{ed}}$, we have a zero matrix block in the lower left corner of the system. As mentioned before, the Butler–Volmer charge transfer kinetics (7) and (12) are implicit with respect to the intercalation and plating currents, and we therefore perform implicit differentiation to consistently linearize the interface conditions (15–17).

As regards the solution of the system (27), we need to be aware of its naturally bad conditioning due to the non-uniform physics involved. More specifically, the anode, the electrolyte, and the cathode of the cell are made of different materials with individual electrochemical transport properties, so that the corresponding mathematical representations, i.e., governing equations and associated model parameters, also have distinct characteristics. For instance, the conservation equations (1) and (5) for lithium mass and electric charge are decoupled with respect to the lithium concentration and electric potential inside the electrode phase, but they are coupled with respect to the two analogous primary variables pertaining to the electrolyte phase. As a consequence, the sparsity pattern of the system exhibits inhomogeneously distributed connections besides being inherently non-symmetric. To give another example, lithium diffusion coefficients are commonly smaller inside the electrode phase than inside the electrolyte phase by many orders of magnitude, while the contrary often holds for the respective electronic and ionic conductivities. Furthermore, the overall lithium concentration field and electric or electrochemical potential field inside the entire cell may be significantly discontinuous across the anode-electrolyte and cathode-electrolyte interfaces. For these reasons, the rows of the system might have very different norms in spite of the scaling of the conservation equations (5) for electric charge by $\frac{1}{F}$.

While all these difficulties might not pose serious numerical challenges to direct linear solvers applicable to small problems, they become significant as soon as larger problems requiring iterative linear solvers are considered. In this case, a successful and efficient solution of the system (27) typically demands powerful, physics-oriented preconditioning prior to the actual solution procedure. For this purpose, we developed a combined row equilibration, block Gauss–Seidel, and algebraic multigrid preconditioning approach based on our previous work presented in [52, 53]. The performance of this approach proved to be very good in a series of numerical experiments. The downstream solution of the system after preconditioning is accomplished by the generalized minimal residual (GMRES) method [54]. In all numerical examples shown in Section 4, we define the GMRES method as converged as soon as the relative L^2 norm of the GMRES residual vector has become smaller than 10^{-8}.

3. Regularization methods

As mentioned in Section 2.2, the interface conditions (15–17) introduce a strong coupling, nonlinearity, and discontinuity to the system (26), making its numerical treatment very challenging. While the monolithic Newton–Raphson scheme established in Section 2.5 is adequate to properly handle the coupling and the nonlinearity, further measures may need to be taken to mitigate the negative impact of the discontinuity
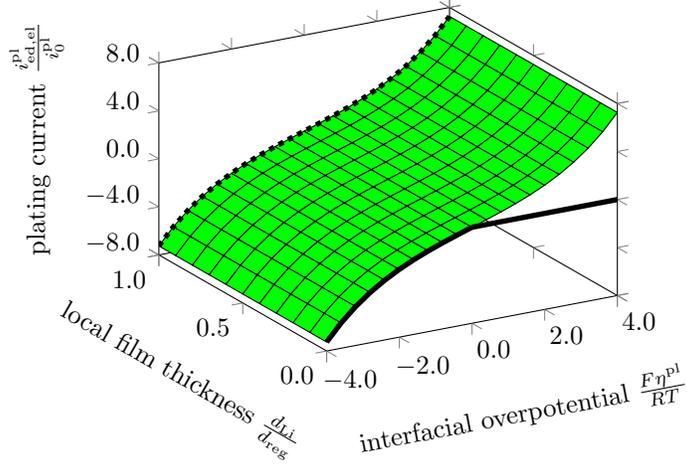
Figure 2: Normalized visualization of the non-regularized plating current (12) for $\alpha_{\mathrm{a}}^{\mathrm{pl}} = \alpha_{\mathrm{c}}^{\mathrm{pl}} = 0.5$.

in the plating current (12) on the convergence behavior of the Newton–Raphson method, see also [6]. To this end, we derive a novel regularization method in the following and compare it to the existing one from [6, 37, 43].

Figure 2 provides a normalized, dimensionless visualization of the non-regularized plating current (12) for $\alpha_{\mathrm{a}}^{\mathrm{pl}} = \alpha_{\mathrm{c}}^{\mathrm{pl}} = 0.5$ as a function of the interfacial overpotential and the local film thickness of plated lithium. The quantity d_{reg} in the axis labeling denotes the regularization length introduced later. The solid black line in the foreground and the dotted black line in the background are both part of the otherwise green function graph. We clearly observe a discontinuity in the plating current along the straight part of the solid black line, i.e., along the detached branch of the function graph, where $\eta^{\mathrm{pl}} > 0$ and $d_{\mathrm{Li}} = 0$. When we charge the cell in the absence of plated lithium, the electrochemical state associated with the plating current evolves along this detached function branch, gradually approaching the separation point at the origin of the coordinate system. As soon as the separation point is reached, the plating condition is fulfilled and a lithium film emerges, causing the electrochemical state to move on in the direction of a decreasing interfacial overpotential and an increasing local film thickness. So far, the discontinuity in the plating current has not yet become noticeable. When we switch from charge to relaxation or discharge in the presence of already plated lithium, the plating current is reversed and lithium stripping is initiated, causing the electrochemical state to shift towards a decreasing local film thickness while maintaining a positive interfacial overpotential. At the critical moment when all plated lithium is consumed and the electrochemical state returns to the detached function branch, the discontinuity in the plating current finally takes effect and lithium stripping is abruptly stopped, i.e., the plating current immediately drops from its full extent to zero. In case this drop happens during discharge and not during relaxation, additional jumps occur simultaneously in the interfacial overpotential and hence also in the intercalation current to compensate for the lost contribution of the plating current to the total electric current density (6) at the anode-electrolyte interface. While these sudden changes in the discharge characteristics of the cell are physical in that lithium stripping naturally stalls at the point where the deposited lithium film is completely depleted, the convergence of the monolithic Newton–Raphson scheme and hence the computational robustness of our entire model may be seriously harmed, as demonstrated in our numerical examples in Sections 4.1.7 and 4.2.4. Other powerful solution schemes besides the monolithic Newton–Raphson scheme are usually also gradient-based and therefore afflicted by this problem as well.

As a remedy, regularization techniques can be applied to the plating current (12) to remove or at least mitigate the discontinuity and its negative impact. The approach originally proposed in [6] and later adopted in [37, 43] introduces a polynomial regularization to the anodic exponential component of the plating current,
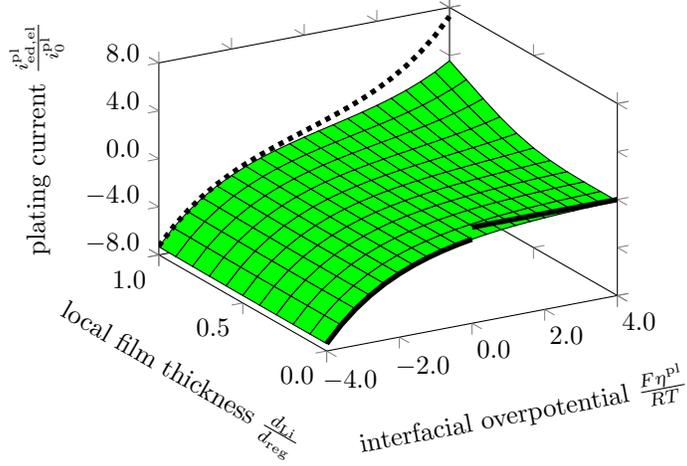
Figure 3: Normalized visualization of the polynomially regularized plating current (28) for $\alpha_a^{pl} = \alpha_c^{pl} = 0.5$.

i.e., to the half reaction associated with lithium stripping:

$$
i_{ed,el}^{pl} = \begin{cases} i_0^{pl} \left(f(d_{Li}, d_{reg}) \exp\left(\frac{\alpha_a^{pl} F \eta^{pl}}{RT} \right) - \exp\left(-\frac{\alpha_c^{pl} F \eta^{pl}}{RT} \right) \right) & \text{if } \eta^{pl} < 0 \text{ or } d_{Li} > 0 \\ 0 & \text{otherwise} \end{cases}
\tag{28}
$$

with the regularization function

$$
f(d_{Li}, d_{reg}) = \frac{d_{Li}^4}{d_{Li}^4 + d_{reg}^4}.
\tag{29}
$$

Herein, the regularization length d_{reg} controls the range of the local film thickness where the regularization is effective. The authors of [6] set d_{reg} to a presumably arbitrary value of $0.48\,\text{nm}$ and comment that smaller values make the numerical treatment of the plating current more challenging, leading to significantly larger solver iteration counts and simulation times. In the limiting case

$$
\lim_{d_{reg} \to 0} f(d_{Li}, d_{reg}) = 1,
\tag{30}
$$

the regularization function becomes unity and the non-regularized plating current (12) is recovered.

A normalized, dimensionless visualization of the regularized plating current (28) for $\alpha_a^{pl} = \alpha_c^{pl} = 0.5$ is provided by Figure 3. The function graph again includes the solid black line in the foreground, but no longer the dotted black line in the background. The latter is merely copied from Figure 2 to facilitate a comparison with the non-regularized plating current (12). We observe that the discontinuity in the plating current for $\eta^{pl} > 0$ and $d_{Li} = 0$ is less pronounced due to the regularization. The resulting numerical method is therefore expected to be more robust at the critical moment when all plated lithium is consumed during relaxation or discharge. On the downside, the discontinuity is still not completely removed and now also becomes noticeable at the origin of the coordinate system, where we detect a newly introduced jump in the solid black line. As a consequence, we may predict that the convergence of the monolithic Newton–Raphson scheme suffers from the regularization at the onset of lithium plating, possibly exhibiting even less computational robustness than without any regularization. Furthermore, the regularization heavily smears the non-regularized function graph from Figure 2 and recovers the dotted black line only asymptotically for $d_{Li} \to \infty$, revealing its highly invasive nature. And lastly, the regularization function (29) lacks physical motivation, besides not always yielding a qualitatively correct discharge behavior. In particular, the plating current is negative in case the interfacial overpotential is positive and the local film thickness is small, so that lithium stripping switches to lithium plating shortly before all plated lithium is consumed. This mechanism is physically implausible and conceptually prevents an already deposited lithium film from being completely
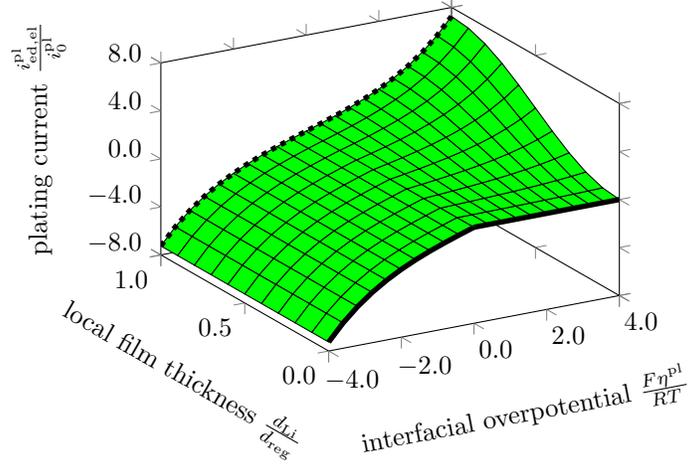
Figure 4: Normalized visualization of the plating current (31) with novel regularization for $\alpha_{\mathrm{a}}^{\mathrm{pl}} = \alpha_{\mathrm{c}}^{\mathrm{pl}} = 0.5$.

dissolved even inside the physical regime of lithium stripping, as demonstrated later in our numerical example in Section 4.1.7.

To address these shortcomings, we propose a novel, alternative regularization variant as follows:

$$i_{\mathrm{ed,el}}^{\mathrm{pl}} = i_0^{\mathrm{pl}} g(d_{\mathrm{Li}}, d_{\mathrm{reg}}, \eta^{\mathrm{pl}}) \left(\exp\left(\frac{\alpha_{\mathrm{a}}^{\mathrm{pl}} F \eta^{\mathrm{pl}}}{RT} \right) - \exp\left(-\frac{\alpha_{\mathrm{c}}^{\mathrm{pl}} F \eta^{\mathrm{pl}}}{RT} \right) \right). \tag{31}$$

Herein, the case differentiation is shifted from the plating current itself to the trigonometrical regularization function

$$g(d_{\mathrm{Li}}, d_{\mathrm{reg}}, \eta^{\mathrm{pl}}) = \begin{cases} 0.5 \left(1 - \cos\left(\frac{\pi d_{\mathrm{Li}}}{d_{\mathrm{reg}}} \right) \right) & \text{if } \eta^{\mathrm{pl}} > 0 \text{ and } d_{\mathrm{Li}} < d_{\mathrm{reg}} \\ 1 & \text{otherwise} \end{cases}. \tag{32}$$

Unlike before, the regularization function now affects both exponential components of the plating current and depends also on the interfacial overpotential. Moreover, the regularization is no longer active within almost the entire infinite domain of the plating current, but it is strictly confined to the section where it is actually needed for discontinuity removal, i.e., where the interfacial overpotential is positive and the local film thickness is below the regularization length.

Figure 4 gives a normalized, dimensionless visualization of our new regularization technique for $\alpha_{\mathrm{a}}^{\mathrm{pl}} = \alpha_{\mathrm{c}}^{\mathrm{pl}} = 0.5$. Both the solid black line in the foreground and the dotted black line in the background, again copied from Figure 2, belong to the function graph of the plating current. We notice that all aforementioned disadvantages of the previous regularization approach are eliminated. Most importantly, the discontinuity is completely gone, i.e., the plating current now evolves continuously both at the beginning of lithium plating and at the end of lithium stripping. Besides, the directional derivative of the function graph with respect to the local film thickness vanishes at the solid and dotted black lines, so that we obtain mathematically smooth transitions around $d_{\mathrm{Li}} = 0$ and $d_{\mathrm{Li}} = d_{\mathrm{reg}}$. The function graph is continuously differentiable everywhere except for the slightly non-smooth kink at $\eta^{\mathrm{pl}} = 0$, where we may adopt countermeasures such as adaptive numerical time stepping if need be. Also, our regularization is minimally intrusive due to its local confinement and therefore does not overly smear the non-regularized function graph from Figure 2. More precisely, the non-regularized function graph is recovered exactly already at $d_{\mathrm{Li}} = d_{\mathrm{reg}}$, and it is not only approached asymptotically for $d_{\mathrm{Li}} \to \infty$. In addition, our regularization is physically reasonable in that the interfacial overpotential and the resulting plating current never have opposite signs. As a consequence, lithium plating and stripping occur exclusively inside their respective physical regimes and are thus captured in a qualitatively correct manner. In particular, we allow already plated lithium to be entirely consumed by lithium stripping without prematurely switching over to lithium plating.
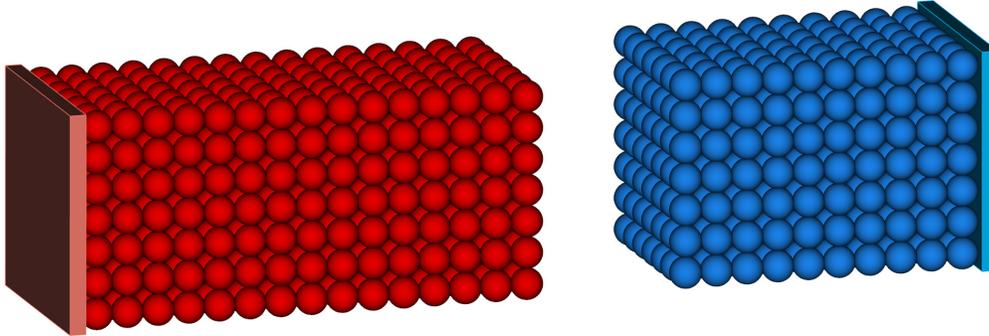
11

Figure 5: Academic lithium-ion cell from [58] with anode (red), cathode (blue), and respective current collectors.

A physical motivation of our regularization function (32) is established by setting the regularization length to the diameter of a lithium atom, i.e., $d_{\mathrm{reg}} = 0.29\,\mathrm{nm}$. In so doing, the regularization-induced slope in the function graph from Figure 4 can be interpreted as a natural deceleration of lithium stripping, initiated at the point where a deposited lithium film has already been reduced to a monolayer of lithium atoms. As more and more parts of the monolayer are subsequently dissolved and therefore no longer contribute to the plating current, lithium stripping gradually ceases and finally comes to an end when all plated lithium is gone. In this sense, our regularization function distinguishes between reactive and inert portions of the anode-electrolyte interface according to its monolayer coverage to decrease the rate constant of lithium stripping in a locally homogenized manner. We remark that our value $d_{\mathrm{reg}} = 0.29\,\mathrm{nm}$ is significantly smaller than the value $d_{\mathrm{reg}} = 0.48\,\mathrm{nm}$ pertaining to the regularization function (29), so that our regularization is not only conceptually, but also quantitatively less intrusive than the previous one.

4. Numerical examples

Having detailed the theoretical framework of our modeling and simulation approach in the previous sections, we now present selected numerical examples to demonstrate its practical applicability and to gain profound insight into the physical mechanisms of lithium plating and stripping. Two different lithium-ion cells are studied, one with academic electrode microstructures consisting of ideally spherical particles, and another one with realistic electrode microstructures reconstructed from X-ray tomography data. Unless stated otherwise, our novel regularization technique with $d_{\mathrm{reg}} = 0.29\,\mathrm{nm}$ is used. All simulations were performed on a parallel computer cluster running BACI [55], our in-house multiphysics research code providing the required finite element implementation. For postprocessing purposes, we employed Kitware ParaView 4.4.0 [56] to visualize physical fields and MATLAB R2017b [57] to plot diagrams.

4.1. Lithium-ion cell with academic electrode microstructures

As a first step, we apply our model to a lithium-ion cell with academic electrode microstructures, taken from [58] and depicted in Figure 5. Both electrodes of the cell are composed of equally sized, closely packed spheres in a cubic lattice, while the voids inside and between the electrodes are filled with electrolyte. The anode and the cathode are $8\,\mu\mathrm{m}$ apart in axial direction and consist of 15 and 10 axially stacked particle layers, respectively. Each spherical particle has a radius of $1\,\mu\mathrm{m}$ and overlaps all adjacent objects by an angle of 30°, see Figure 6 for a schematic illustration.

Due to the regular arrangement of the electrode particles, we can imagine the cell to be symmetrically and infinitely mirrored in lateral direction. The smallest recurring unit of the cell has the shape of a right triangular prism, reaching from one current collector to the other and capturing an eighth of one axial particle row with 15 anode particles and 10 cathode particles, whose spherical surfaces are slightly truncated in the lateral overlap regions. To maximize computational efficiency, we exclusively consider this minimal domain
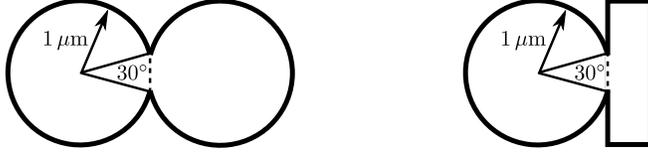
12

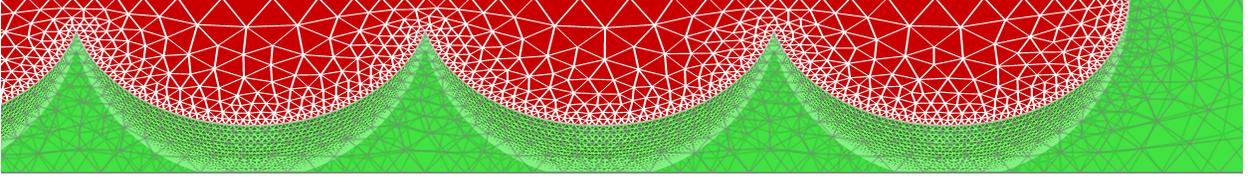Figure 6: Particle radius and overlap angle.

Figure 7: Three meshed anode particles with increased mesh resolution towards the anode-electrolyte interface.

in the following, and we adopt csimsoft Trelis Pro 15.2.2 [59] to generate the corresponding geometry and finite element mesh.

Figure 7 shows the three meshed anode particles closest to the cathode. For a better resolution of the complex interface phenomena described in Sections 2.2 and 3, the mesh is significantly refined towards the anode-electrolyte and cathode-electrolyte interfaces. Altogether, the mesh involves around 140,000 finite element nodes, 610,000 finite elements, and 300,000 degrees of freedom. We have slightly more than exactly twice as many degrees of freedom as finite element nodes due to the supplementary degrees of freedom associated with the local film thickness at the anode-electrolyte interface. Since the total number of degrees of freedom is too large for direct linear solvers to be feasible, we employ the iterative linear solver from Section 2.5 in a parallelized setting on 8 CPUs.

The model parameters adopted for our subsequent simulations were originally determined for the so-called FreedomCAR cell [44, 58] exhibiting a graphite anode and an NCA cathode, see Appendix A for details. Since the total capacity of the anode exceeds the one of the cathode by about 12.4% based on the cell geometry and the values of $c_{\mathrm{ed}}^{0\%}$ and $c_{\mathrm{ed}}^{100\%}$ given by Table A.1, the cathode constitutes the limiting electrode and, as such, defines the state of charge of the whole cell. Concerning time discretization and integration, we perform adaptive numerical time stepping with a main time step size of $1.0\,\mathrm{s}$ and a reduced time step size of $0.2\,\mathrm{s}$. The latter is employed only around initial occurrences of lithium plating and around reversals of the overall electric current during cycling to ensure a good temporal resolution of these critical simulation phases. No time step size refinement is required around final stages of lithium stripping when all plated lithium is dissolved, since critical transients resulting from lithium stripping are prevented by our novel regularization technique from Section 3.

4.1.1. Validation

Before considering lithium plating and stripping, we validate our basic finite element implementation by replicating a series of discharge characteristics from [58]. To this end, we modify the initial lithium concentrations from Table A.1 in such a way that we start with a fully charged cell at 100% state of charge. We first simulate a complete discharge process at a discharge rate of $1\,\mathrm{C}$, depleting the state of charge of the cell from 100% to 0% within one hour. The overall cell potential difference, i.e., the absolute difference between the electric potentials averaged over each of the two contact surfaces $\Gamma_{\mathrm{cc,a}}$ and $\Gamma_{\mathrm{cc,c}}$ from Figure 1, is recorded during the simulation and visualized in Figure 8 along with the corresponding reference solution from [58]. Analogous comparisons are then drawn also for a higher discharge rate of $5\,\mathrm{C}$ and for alternative overlap angles of $15°$ and $45°$ instead of the original overlap angle of $30°$ from Figure 6. Though not explicitly shown as well, the results produced by all of our simulations are qualitatively as close to the respective reference results from [58] as in Figure 8, so that the basic validity of our implementation is successfully confirmed. The minor discrepancies in the results at low states of charge of the cell may be attributed
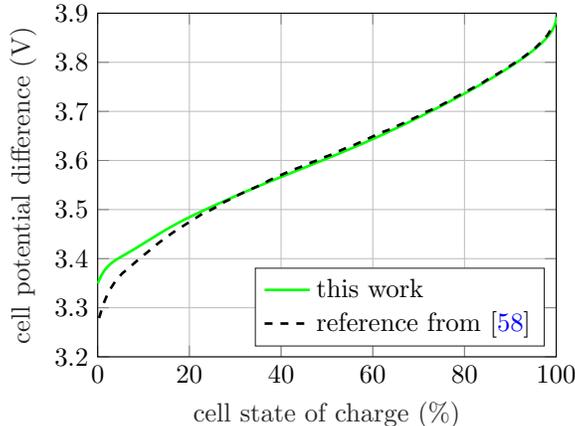
Figure 8: Validation of basic finite element implementation without lithium plating and stripping.

to methodological differences between our implementation and the one from [58], especially regarding the discretization and solution of the governing equations. For instance, the discretization technique from [58] involves a second-order finite volume scheme solving the governing equations in a partitioned manner.

4.1.2. Influence of operating conditions on lithium plating and stripping

Next, we incorporate our modeling and simulation approach to lithium plating and stripping into our finite element implementation to study the charge and discharge behavior of the cell under different operating conditions. We thereby demonstrate that our approach is sensitive to all three major causes of lithium plating, i.e., that it reliably predicts lithium plating induced by overcharging, fast charging, and low-temperature charging.

Figure 9 illustrates the charge and discharge behavior of the cell in the case of overcharging. More precisely, the overall cell potential difference is plotted as a function of the state of charge of the cell for five different charge rates ranging from 5 C to 9 C in steps of 1 C. Each simulation starts with a completely discharged cell at 0% state of charge without any plated lithium, see Section 2.3 and Table A.1. From this initial state, the cell is galvanostatically charged beyond 100% state of charge at the indicated charge rate, following the upper branch of each curve. As soon as a relatively high upper cutoff voltage of 6 V is reached, the overcharging of the cell is terminated. The cell then enters a relaxation phase with a duration of 30 s, as captured by the fully vertical curve segment, before being discharged at a reduced rate of 1 C until returning to 0% state of charge along the lower branch of each curve. Thus, we record each curve in clockwise direction during one single simulation, starting and finishing at the lower left corner of the diagram.

While the curves associated with the five different charge rates all look qualitatively similar, we notice that an increase in the charge rate leads to a decrease in the maximum state of charge of the cell at the upper cutoff voltage, i.e., higher rates of overcharging result in lower degrees of overcharging, and vice versa. Moreover, a closer look at the curves reveals a kink along the upper branch of each curve. This kink indicates the onset of lithium plating and has been similarly observed in past experiments and simulations, see, e.g., [21, 37]. At the point where lithium plating starts, the plating current begins to contribute to the total electric current density at the anode-electrolyte interface, thereby initiating a decrease in the magnitude of the intercalation current and hence also a change in the temporal evolution of both the corresponding interfacial overpotential and the overall cell potential difference as a whole. For the 9 C charge rate, a close-up of the kink at around 100% state of charge of the cell is provided. With decreasing charge rate, the kink is shifted in top right direction, implying that lithium plating occurs later during charging and may therefore be considered less likely. These findings are physically plausible and in line with common expectations, proving the essential validity of our approach and its implementation.

Additional insight into the charge and discharge behavior of the cell in the presence of lithium plating and
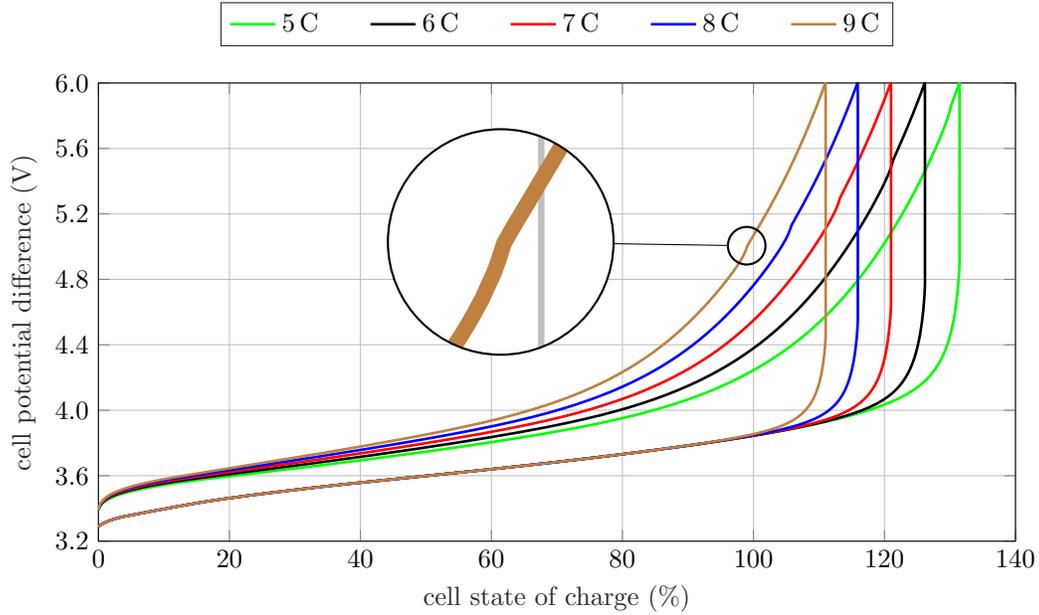
14

Figure 9: Cell potential difference as a function of the cell state of charge in the case of overcharging.
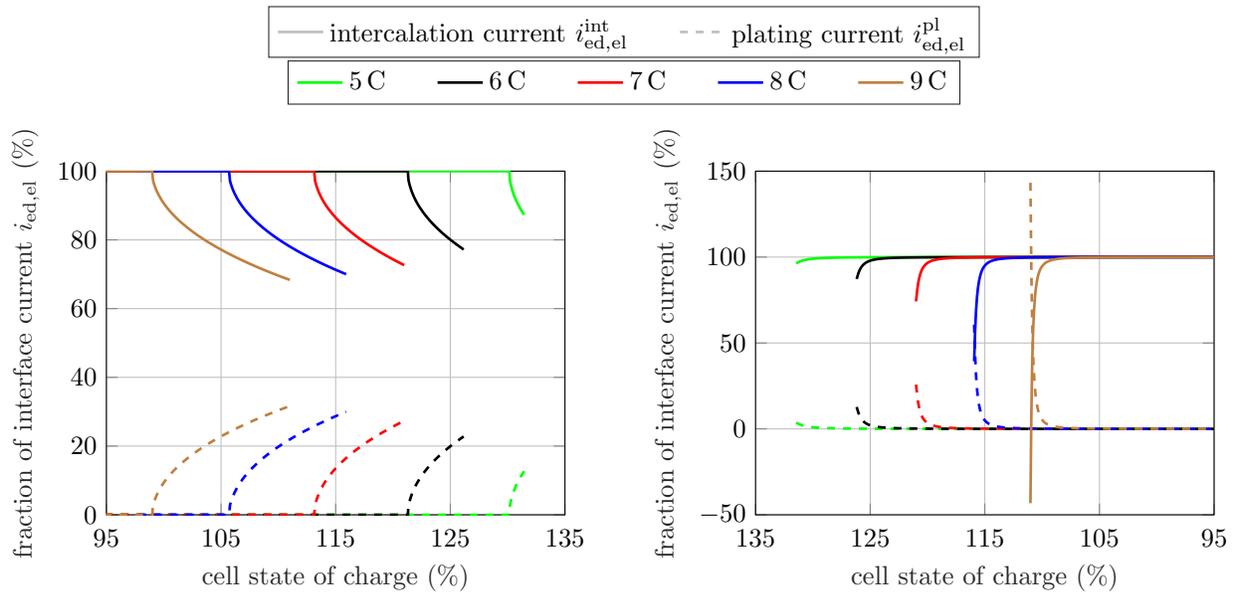

Figure 10: Intercalation versus plating current during charge (left) and discharge (right) in the case of overcharging.
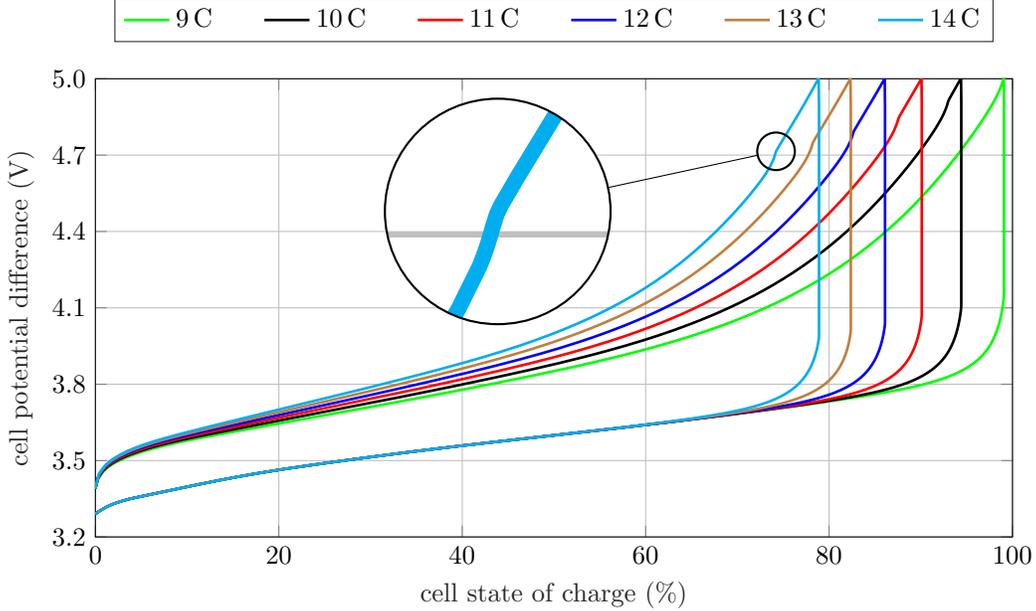
15

Figure 11: Cell potential difference as a function of the cell state of charge in the case of fast charging.

stripping is given by Figure 10, where the five previous simulations are further analyzed. In particular, the breakdown (6) of the total electric current density at the anode-electrolyte interface is quantified in terms of percentage fractions associated with the intercalation and plating currents. The left and right panels capture lithium plating towards the end of the charge process and lithium stripping at the beginning of the discharge process, respectively. The relaxation phase between the charge and discharge processes is omitted. The solid curves pertain to lithium intercalation in the left panel and to lithium deintercalation in the right panel, while the dashed curves refer to lithium plating in the left panel and to lithium stripping in the right panel.

We observe that the plating current makes an increasing contribution to the total electric current density at the anode-electrolyte interface from the start of lithium plating onward in each simulation, thereby producing the aforementioned kink in the curve describing the overall cell potential difference as a function of the state of charge of the cell. As expected, higher charge rates result in more pronounced lithium plating and stripping, as indicated by the larger percentage fractions reached by the corresponding dashed curves. In the case of the $9\,C$ charge rate, the lithium stripping fraction even exceeds 100% at the beginning of the discharge process, while the complementary lithium deintercalation fraction falls below 0% accordingly. In other words, the intercalation current and the associated interfacial overpotential are negative, whereas the plating current and the associated interfacial overpotential are positive. The difference in the signs is primarily due to the offset Φ_0^{int} between the two interfacial overpotentials, see their respective definitions (9) and (14). We deduce that the lithium film deposited during the preceding charge process is dissolved in two different ways: One portion of lithium migrates from the anode to the cathode to discharge the cell, and the other portion enters the anode through local lithium intercalation, so that the amount of intercalated lithium inside the anode temporarily increases in spite of the cell being globally discharged. As soon as the lithium stripping fraction drops below 100% and the lithium deintercalation fraction becomes positive, local intercalation of plated lithium ceases and lithium deintercalation sets in, causing lithium to move from the anode to the cathode along with lithium stripping. As the discharge process continues, lithium deintercalation plays a more and more dominant role, while the lithium stripping fraction gradually goes down and vanishes eventually.

Having investigated the effect of overcharging on lithium plating and stripping, we now turn our attention
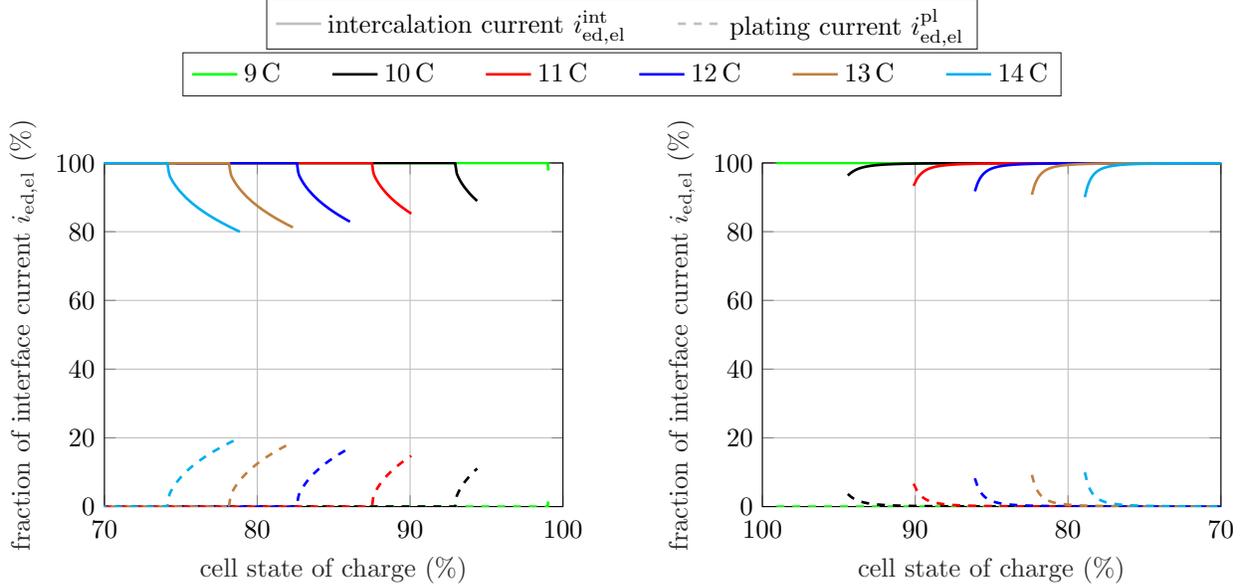
Figure 12: Intercalation versus plating current during charge (left) and discharge (right) in the case of fast charging.

to fast charging as a second major cause of lithium plating. For this purpose, we consider Figures 11 and 12, where the charge and discharge behavior of the cell is displayed for high charge rates from $9\,\mathrm{C}$ to $14\,\mathrm{C}$ in steps of $1\,\mathrm{C}$. The diagrams are analogous to the ones shown in Figures 9 and 10 from the preceding discussion on overcharging. Each simulation is specified in the same way as before, except that the upper cutoff voltage is reduced from $6\,\mathrm{V}$ to $5\,\mathrm{V}$ to no longer induce any overcharging of the cell beyond 100% state of charge.

Again, we observe qualitative similarity between all curves in each diagram and confirm that increasing the charge rate decreases the maximum state of charge of the cell at the upper cutoff voltage. Since the charge rates are overall higher than before, lithium plating and stripping already occur below 100% state of charge of the cell, and reducing the charge rate once more shifts the kink along the upper branch of each curve further in top right direction. As regards the intercalation and plating current fractions, raising the charge rate again reinforces lithium plating and stripping. At the lowest charge rate of $9\,\mathrm{C}$, lithium plating arises only at the very end of the charge process, and the small amount of plated lithium is almost entirely consumed by intercalation into the anode during the relaxation phase, so that there is no measurable plating current even at the start of the discharge process. At the other extreme, even the maximum charge rate of $14\,\mathrm{C}$ is not enough anymore to trigger local intercalation of plated lithium at the beginning of the corresponding discharge process. Instead, the intercalation and plating current fractions both lie between 0% and 100% all the time, implying that the discharge process involves lithium deintercalation along with lithium stripping right from the beginning.

Finally, we focus on low-temperature charging as the last major cause of lithium plating by examining Figures 13 and 14, where the diagrams are again analogous to the ones shown before and reflect the charge and discharge behavior of the cell at low temperatures from $258\,\mathrm{K}$ to $278\,\mathrm{K}$ in steps of $2.5\,\mathrm{K}$. Most of the previous model parameters are reused, including the reduced upper cutoff voltage of $5\,\mathrm{V}$. However, we replace the varying charge rates by a unified, comparatively small charge rate of $2\,\mathrm{C}$ to clearly dissociate low-temperature charging from overcharging and fast charging. Besides, each discharge process is terminated as soon as a lower cutoff voltage of $3\,\mathrm{V}$ is reached, even if the state of charge of the cell is still greater than 0%.

As before, we notice that all curves in each diagram look qualitatively the same. According to physical intuition, the maximum state of charge of the cell at the end of the charge process decreases with temperature. In every simulation, lithium plating and stripping occur within the regime below 100% state of charge of
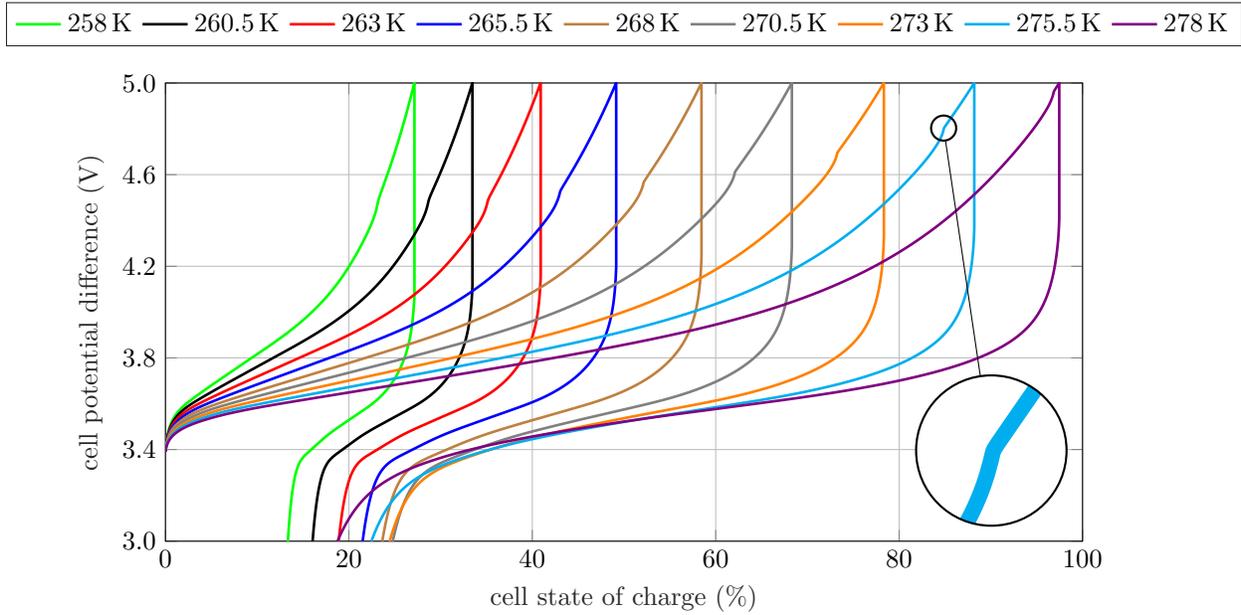
17

Figure 13: Cell potential difference as a function of the cell state of charge in the case of low-temperature charging.
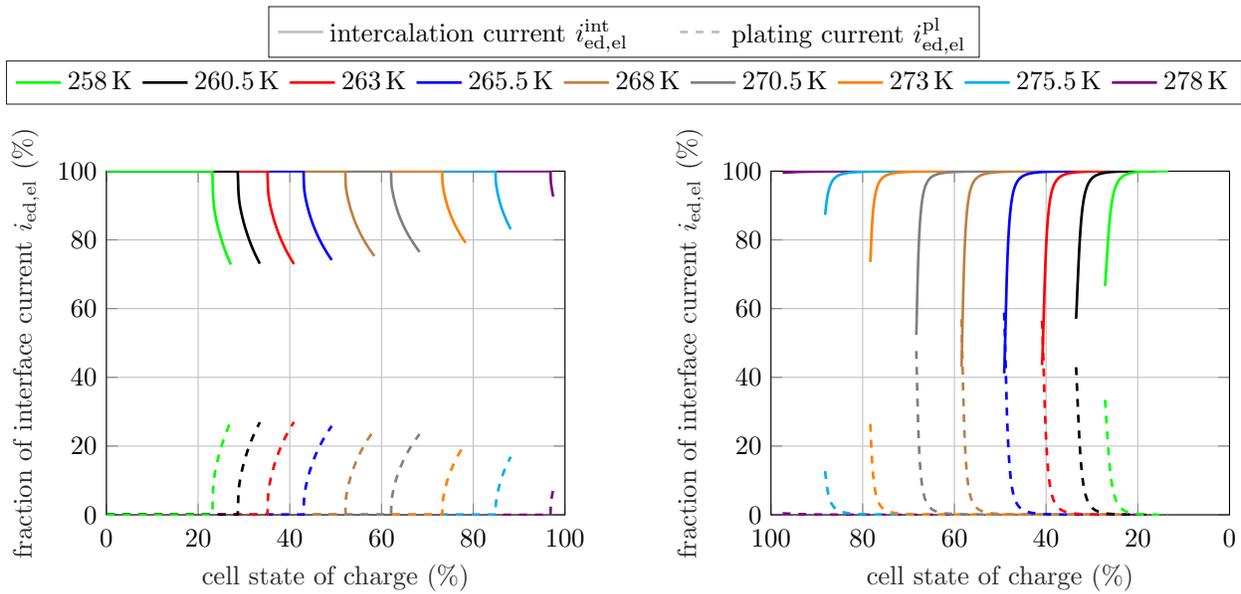

Figure 14: Intercalation versus plating current during charge (left) and discharge (right) in the case of low-temperature charging.
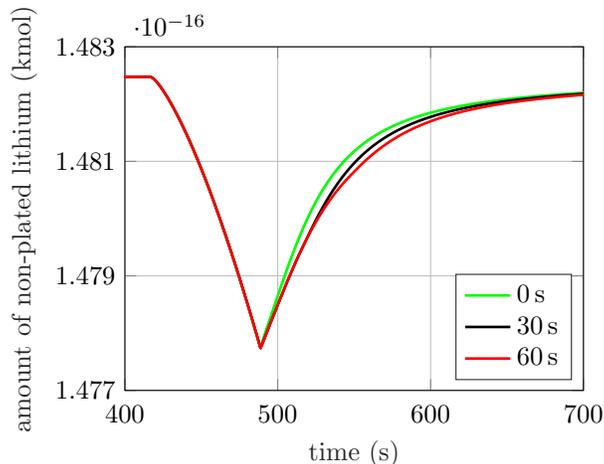
Figure 15: Amount of non-plated lithium during lithium plating and stripping involving relaxation times of 0 s, 30 s, and 60 s.

the cell, and increasing the temperature shifts the onset of lithium plating to larger overall cell potential differences and states of charge of the cell as expected. Again, we do not observe local intercalation of plated lithium at the beginning of the discharge process in any of the simulations. However, we deduce from Figure 14 that the intensity of lithium plating and stripping is no longer monotonic across all simulations, but less pronounced at low and high temperatures while being stronger in between. In addition to the curves in the diagrams, our simulation results analogously show that the maximum local film thickness of plated lithium at the end of the charge process is smaller at low and high temperatures than at intermediate ones. This phenomenon is due to coupled interactions between the various nonlinearities in our model, paired with the usage of the same upper cutoff voltage in all simulations. At low temperatures, we quickly hit this upper cutoff voltage already at small states of charge of the cell, so that lithium plating is stopped early before building up large local film thicknesses.

4.1.3. Impact of the relaxation time on lithium stripping

We now investigate the sensitivity of lithium stripping to the duration of the relaxation phase between charging and discharging the cell. The three curves in Figure 15 are associated with the 258 K simulation analyzed in Figures 13 and 14. While the black curve represents the original simulation involving a relaxation time of 30 s, the green and red curves correspond to analogous simulations with modified relaxation times of 0 s and 60 s, respectively. Each curve illustrates the temporal evolution of the total amount of non-plated lithium inside the entire cell during lithium plating and stripping.

After a little more than 400 s, the onset of lithium plating causes the three initially horizontal lines to bend downwards, as the emerging lithium film starts to consume non-plated lithium. At the end of the charge process shortly before 500 s, the lithium film reaches its maximum thickness, so that the amount of non-plated lithium exhibits a minimum accordingly. At this point, the green curve immediately runs into the discharge process, whereas the black and red curves both enter the relaxation phase. We observe that all three curves instantly begin to go back up again, implying that plated lithium is dissolved by discharge as well as relaxation. A closer look at the kink reveals that the green curve branches off the two other ones with a steeper slope, since lithium stripping occurs faster during discharge than during relaxation. As soon as the first 30 s of the relaxation phase have passed, the black curve also hits the beginning of the discharge process and separates from the red curve in a way similar to the green curve. Another 30 s later, the red curve finally transitions from relaxation to discharge as well. In all three simulations, the lithium film is almost completely gone after 700 s, where the depicted time period ends.

Overall, increasing the duration of the relaxation phase between charging and discharging the cell generally decelerates lithium stripping from the beginning of the relaxation phase onward, up to the point where
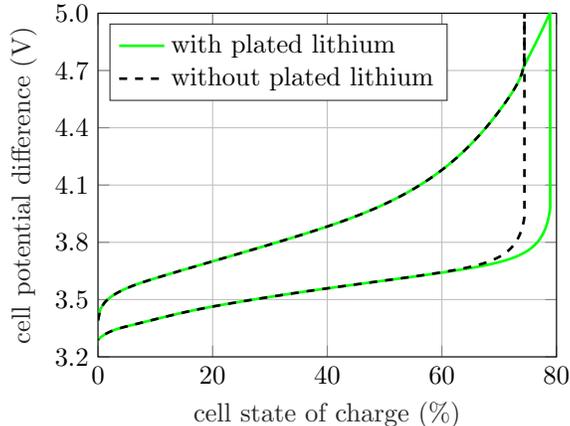
19

Figure 16: Cell potential difference as a function of the cell state of charge with and without lithium plating and stripping.

all plated lithium is dissolved during relaxation and even longer relaxation times do not make any further difference to lithium stripping.

4.1.4. Cycling behavior with and without lithium plating and stripping

The impact of lithium plating and stripping on the charge and discharge characteristics of the cell is visualized in Figure 16. The solid, green curve is a copy of the curve associated with $14\,C$ charging from Figure 11, whereas the dashed, black curve results from a very similar simulation with the only difference that lithium plating and stripping are suppressed. We observe that the physical mechanisms of lithium plating and stripping have a noticeable effect on the cycling behavior of the cell. Without lithium plating and stripping, the overall cell potential difference instantly shoots up as soon as the anode is saturated with lithium underneath its surface towards the end of the charge process, given that the interfacial exchange current density (8) pertaining to the intercalation current approaches zero and thus causes the corresponding interfacial overpotential to diverge under the constant charge rate. On the other hand, the deposition of excess lithium on the anode surface leads to a kink and subsequent flattening of the curve according to our discussion from Section 4.1.2. As a consequence, the upper cutoff voltage is reached significantly later, i.e., at a much higher state of charge of the cell. After the reversal of the overall electric current from charge to discharge, the gap between both curves shrinks and eventually vanishes around 60% state of charge of the cell. We remark that the simulation of the imaginary scenario without lithium plating and stripping requires several consecutive time step refinements towards the end of the charge process to successfully capture the very steep, almost vertical increase in the overall cell potential difference.

4.1.5. Correlation between the distribution of plated lithium and the ionic conductivity of the electrolyte

In the following, we conduct a parametric study of the correlation between the spatial distribution of plated lithium and the ionic conductivity κ_{el} of the electrolyte. For this purpose, we repeatedly rerun the $14\,C$ simulation from Figures 11 and 12, successively downscaling the model parameter A_{el} from Table A.2, and hence also κ_{el} according to the constitutive equation (4), by factors ranging from $10^{-0.5}$ to $10^{-2.5}$ in multiplicative steps of $10^{-0.5}$.

An analysis of the simulation results is given by Figure 17, where the spatial distribution of plated lithium is characterized for each simulation in the series. More precisely, we only consider the time instant at the end of the charge process in each simulation, and we identify the corresponding range of values for the local film thickness of plated lithium at the anode-electrolyte interface. Naturally, the maximum local film thickness is observed where the anode-electrolyte interface is closest to the cathode, i.e., at the cathode-side end of the anode. Lithium ions migrating from the cathode to the anode during the charge process arrive there first, so that the magnitudes of the interfacial overpotential (9) and of the resulting intercalation current are largest.
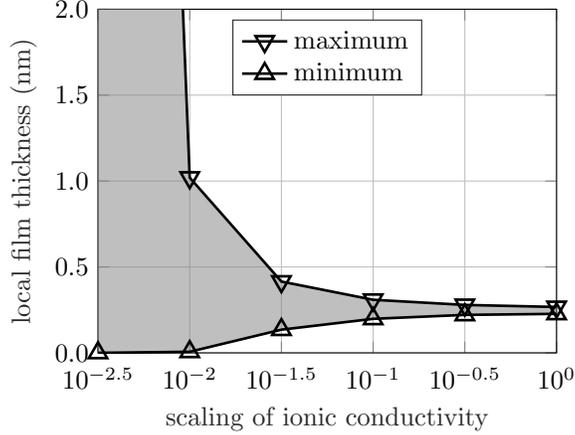
20

Figure 17: Minimum and maximum local film thickness of plated lithium at the end of the charge process as a function of κ_{el}.
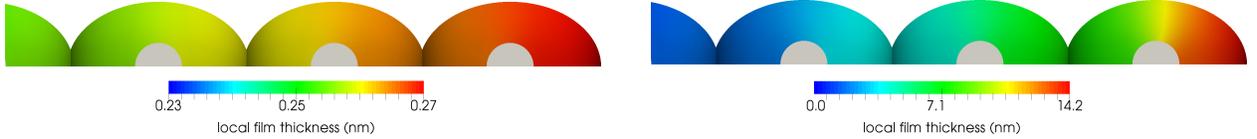

Figure 18: Spatial distribution of plated lithium on the anode surface for ionic conductivities κ_{el} (left) and $\kappa_{el} \times 10^{-2.5}$ (right).

As a consequence, the maximum saturation concentration of intercalated lithium is reached earliest, and the occurrence of lithium plating is quickest and most pronounced. Conversely, the minimum local film thickness is found where the anode-electrolyte interface is farthest away from the cathode, i.e., where it touches the anode-side current collector.

We notice that the original simulation without any downscaling of κ_{el} exhibits a very small range of local film thickness values at the end of the charge process, implying that all plated lithium is rather homogeneously distributed throughout the anode-electrolyte interface without any significant variation in the local film thickness. As κ_{el} decreases, the range of local film thickness values progressively diverges in the shape of a horizontal funnel in the diagram, indicating a more and more inhomogeneous lithium distribution with increasing spatial gradients in axial direction. This phenomenon is in line with physical intuition, given that reducing κ_{el} impairs the mobility of lithium ions inside the electrolyte phase, thus impeding their percolation through the anode microstructure in axial direction. As a result, most plated lithium is deposited on top of the front anode particles closest to the cathode, while only few lithium ions penetrate the anode and travel to the back particles near the anode-side current collector. The strongest downscaling of κ_{el} by the factor $10^{-2.5}$ even leads to a minimum local film thickness of zero, i.e., to an incomplete lithium film covering only the front part of the anode surface. Generally speaking, lowering κ_{el} makes lithium plating start sooner, but the percolation of plated lithium through the anode takes longer at the same time. We remark that the entire charge process requires around 200 s in each simulation and ends slightly earlier as κ_{el} becomes smaller, since the larger ionic resistance of the electrolyte causes the upper cutoff voltage to be reached faster.

Further evidence of our findings is provided by Figure 18, where the spatial distributions of plated lithium visualized in the left and right panels correspond directly to the ranges of local film thickness values from Figure 17 for the original and most strongly downscaled κ_{el}, respectively. Although each panel only captures the three anode particles closest to the cathode, the associated color bar is scaled based on the entire anode surface. The depicted lithium distributions confirm that choosing the original κ_{el} results in rather homogeneous lithium plating throughout the anode-electrolyte interface with only little spatial variation in the local film thickness in axial direction, whereas reducing κ_{el} causes the anode surface to exhibit a local
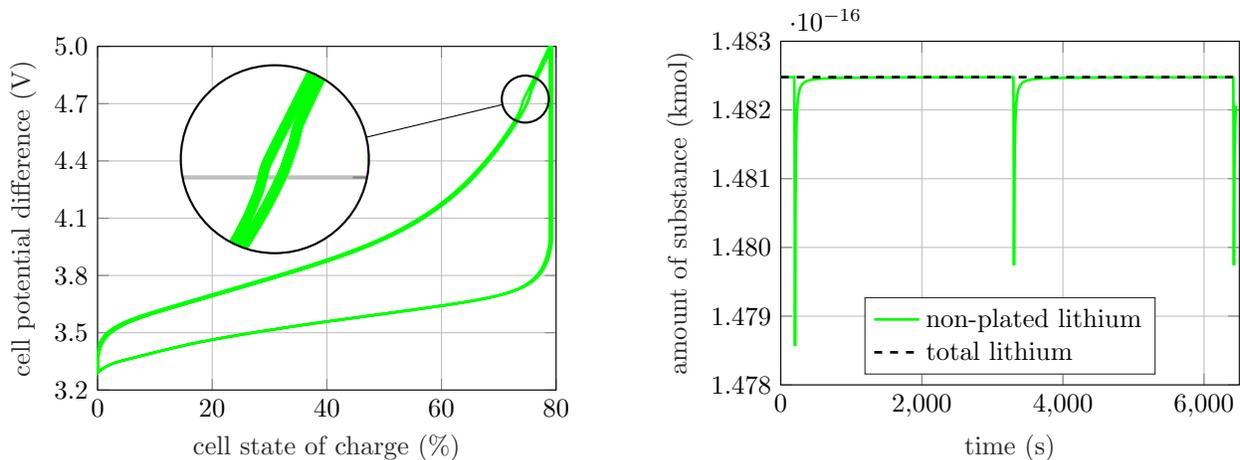
21

Figure 19: Cell potential difference (left) and amounts of non-plated and total lithium (right) during five half cycles.

accumulation of plated lithium at the cathode-side end and no plated lithium at all towards the anode-side current collector.

All in all, we conclude that the characteristics of lithium plating are significantly affected by κ_{el}. The smaller κ_{el} is, the worse becomes the risk of localized lithium plating at the cathode-side end of the anode. Therefore, electrolytes with high κ_{el} are favorable regarding the prevention of lithium plating during cycling.

4.1.6. Continuous cycling involving lithium plating and stripping

To demonstrate that our modeling and simulation approach is capable of repeatedly capturing lithium plating and stripping during one single simulation without any interruptions, we once again reconsider the 14 C simulation from Figures 11 and 12. While the original simulation involves only two half cycles, i.e., one charge process followed by one discharge process, we now extend the run time of the simulation by three additional half cycles, so that three charge processes alternate with two discharge processes. We terminate each discharge process as soon as the state of charge of the cell reaches 0%. A relaxation phase with a duration of 30 s is incorporated not only after each charge process, as was done before, but also after each discharge process.

Figure 19 allows us to thoroughly study the cycling behavior of the cell in the presence of lithium plating and stripping. The left panel illustrates the overall cell potential difference as a function of the state of charge of the cell and closely resembles Figure 16, where only the first two of the five half cycles are recorded. The right panel is similar to Figure 15 and depicts the temporal evolution of the amounts of non-plated and total lithium inside the entire cell. We observe that the solid, green curve associated with non-plated lithium exhibits three localized, downward spikes, each caused by lithium plating and stripping according to the discussion from Section 4.1.3. By contrast, the dashed, black line remains exactly horizontal throughout the simulation, indicating a constant amount of total lithium over time and hence a global conservation of lithium mass as expected. The amounts of non-plated and total lithium differ from each other only in the immediate vicinity of each spike, implying that lithium stripping is accurately captured and completely dissolves all plated lithium without any residual artifacts, as will be further examined in the next section.

A closer look at the right panel reveals that the magnitudes of the second and third spikes are indistinguishable, whereas the first spike is clearly more pronounced. Correspondingly, we deduce from the left panel that lithium plating starts slightly earlier, i.e., at a lower state of charge of the cell, during the first half cycle than during the third and fifth half cycles, resulting in a larger amount of plated lithium at the end of the half cycle. This hysteresis can be explained as follows: At the beginning of the first half cycle, the lithium concentration field inside the anode is spatially constant according to the initial condition (24). After discharging the cell during the second half cycle, the lithium concentration is higher in the interior of the anode and lower towards the anode-electrolyte interface as a consequence of lithium deintercalation.
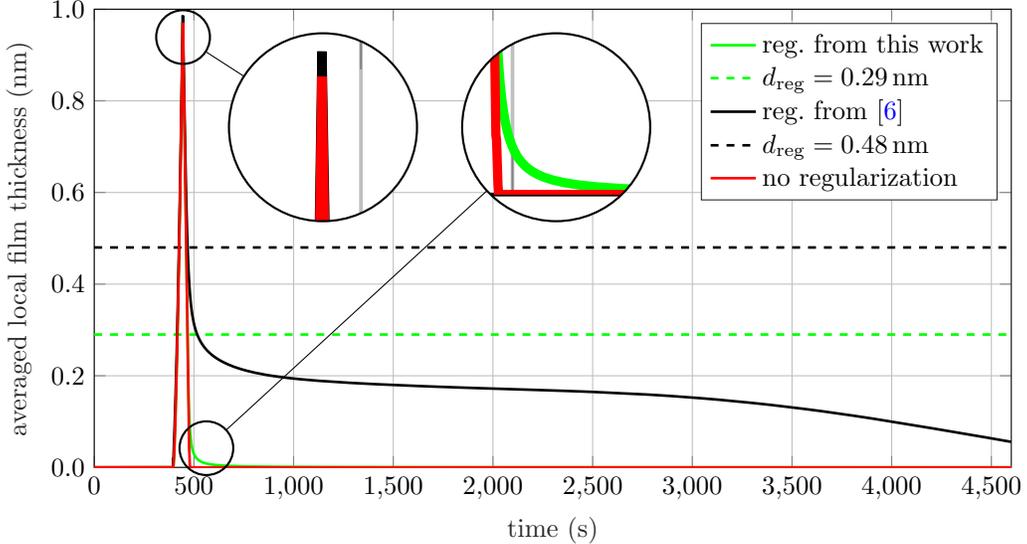
22

Figure 20: Spatially averaged film thickness of plated lithium during charge and discharge with and without regularization.

Although these spatial gradients of the lithium concentration are reduced during the relaxation phase at the end of the second half cycle, they are not fully evened out due to the limited relaxation time. The third half cycle thus starts with a spatially inhomogeneous lithium concentration field inside the anode, where the lithium concentration at the anode-electrolyte interface is significantly lower than at the beginning of the first half cycle. Therefore, the maximum saturation concentration of intercalated lithium at the anode-electrolyte interface is reached later, i.e., at a higher state of charge of the cell, and lithium plating is overall less pronounced. The fifth half cycle, in turn, does not noticeably differ from the third one, since the transient perturbation induced by the initial condition (24) has already been damped out until then, so that the cycling behavior of the cell has become uniformly periodic.

4.1.7. Effect of regularization on lithium plating and stripping

To conclude the investigation of the present lithium-ion cell with academic electrode microstructures, we rerun the 9 C simulation from Figures 9 and 10 twice. Referring to our discussion from Section 3, we replace our novel regularization technique with $d_{reg} = 0.29$ nm by the existing one from [6] with $d_{reg} = 0.48$ nm in the first rerun, whereas no regularization is employed at all in the second rerun. In accordance with our predictions based on Figures 2 and 3, the monolithic Newton–Raphson scheme suffers from severe convergence issues at the onset of lithium plating in the first rerun and at the final stages of lithium stripping in the second rerun, requiring as many as 956 and 37 Newton–Raphson iteration steps per time step for convergence, respectively. By comparison, the original simulation involving our novel regularization technique exhibits, at most, 6 Newton–Raphson iteration steps per time step throughout the run time. The improved convergence behavior and the resulting gains in computational robustness and efficiency are even more evident in our later simulations, and we therefore postpone an in-depth examination until Section 4.2.4.

Lithium plating and stripping during the original simulation and both reruns are analyzed and compared in Figure 20, where the local film thickness of plated lithium, spatially averaged over the entire anode-electrolyte interface, is plotted as a function of time. Each of the three simulations captures a total time period of slightly more than 4,600 s, covering a charge process, a relaxation phase, and a discharge process with durations of nearly 400 s, 30 s, and nearly 4,200 s, respectively. Lithium plating and stripping translate into a distinct, upward spike in each curve, indicating the deposition and dissolution of plated lithium at the anode-electrolyte interface.

The red spike recorded during the simulation without any regularization is most localized, exhibiting
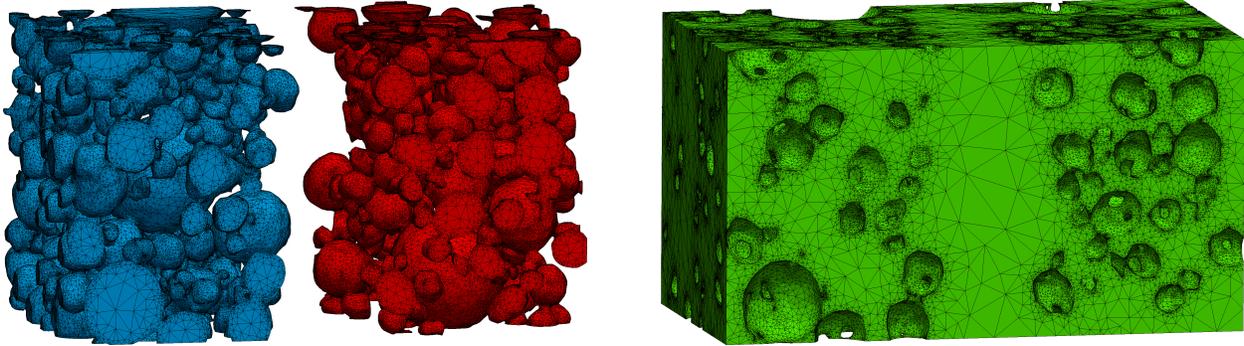
23

Figure 21: Meshed cathode (blue), anode (red), and electrolyte (green) of realistic lithium-ion cell.

sharp edges at the beginning of lithium plating and at the end of lithium stripping. The green spike produced by our regularization is very similar to the red one, proving that our regularization is minimally intrusive and hence conceptually favorable due to its local confinement to small local film thicknesses below $d_{\mathrm{reg}} = 0.29\,\mathrm{nm}$, as discussed in Section 3. The maximum value of the spatially averaged local film thickness at the end of the charge process lies well beyond $d_{\mathrm{reg}} = 0.29\,\mathrm{nm}$, as marked by the dashed, green line in the diagram, implying that lithium plating and stripping are largely unaffected by our regularization. While the red and green spikes are exactly identical both throughout lithium plating and during the early stages of lithium stripping by construction of our regularization, they differ very marginally towards the end of lithium stripping, where the sharp edge of the red spike is artificially smeared and thus transformed into the smooth rounding of the green spike. Although not visible in the diagram, the smearing starts already shortly before the spatially averaged local film thickness is reduced to $d_{\mathrm{reg}} = 0.29\,\mathrm{nm}$ during lithium stripping, since the spatial distribution of plated lithium is inhomogeneous throughout the anode-electrolyte interface, causing our regularization to be activated earlier where the local film thickness is smaller.

In stark contrast to the green spike, the black spike associated with the regularization from [6] deviates from the red spike very early and significantly, revealing the highly intrusive nature of the regularization in agreement with our discussion from Section 3. More specifically, the ambit of the regularization is no longer confined to small local film thicknesses during lithium stripping, but extends to the entirety of the black spike throughout lithium plating and stripping. One visible effect of the regularization is the increased total height of the black spike in comparison to the red and green ones, as highlighted by the corresponding close-up in the diagram. This discrepancy is a consequence of the regularization function (29) inhibiting lithium stripping and hence favoring lithium plating according to the definition (28) of the regularized plating current. Moreover, the physically inconsistent formulation of the regularization causes lithium stripping to considerably decelerate and prematurely stall long before all plated lithium is consumed, so that a residual amount of plated lithium still remains at the anode-electrolyte interface even after completion of the discharge process at the end of the simulation. These unphysical artifacts hinder the regularization from accurately capturing lithium plating and, even more so, lithium stripping.

4.2. Lithium-ion cell with realistic electrode microstructures

The second lithium-ion cell examined in this work is composed of realistic electrode microstructures derived from X-ray tomography data. The resulting geometric and numerical complexity serves to demonstrate that our modeling and simulation approach can be successfully applied not only to academic problem setups, but also to demanding real-world scenarios.

Figure 21 shows the meshed electrode and electrolyte phases of the cell, whose overall axial and lateral dimensions are $360\,\mu\mathrm{m}$ and $200\,\mu\mathrm{m}$, respectively. The axial thickness of either electrode amounts to roughly $160\,\mu\mathrm{m}$, so that the electrolyte volume between both electrodes exhibits an approximate axial length of $40\,\mu\mathrm{m}$. Unlike before, the computational domain is now geometrically irregular, so that it is no longer possible to reduce its size by exploiting internal symmetries, and to thereby enhance computational efficiency. A

24

significant refinement of the mesh towards the anode-electrolyte and cathode-electrolyte interfaces again grants a better resolution of lithium intercalation, deintercalation, plating, and stripping. Altogether, the mesh includes around 1.1 million finite element nodes, 3.9 million finite elements, and 2.3 million degrees of freedom. As discussed earlier, we have slightly more than exactly twice as many degrees of freedom as finite element nodes due to the additional degrees of freedom for the local film thickness. Given that the total number of degrees of freedom is much larger than in the previous problem setup, we increase the number of parallelized CPUs from 8 to 63 accordingly, maintaining a comparable number of degrees of freedom per CPU. The iterative linear solver from Section 2.5 is still employed in all simulations presented in the following.

The X-ray tomography data yielding the electrode microstructures of the cell was adopted from [60], where scans of NMC cathodes were crafted and then provided online with open-source access. Since the literature does not offer any freely available, comprehensive tomography images of anodic microstructures to the best of our knowledge, we reconstructed both the anodic and the cathodic microstructure of the cell from the published scans of NMC cathodes. To this end, we used Materialise Mimics 16.0 [61] to digitally transform the tomography data into a large, three-dimensional microstructure, where we cut out two individual, characteristic blocks for the two electrodes of the cell. Afterwards, we manually edited both blocks with Materialise 3-matic 8.0 [62] in an extensive and careful manner to assemble the cell and to discretize its surface by a high-quality, triangular mesh with well-shaped finite elements. This surface mesh was finally loaded into Gmsh 2.9.3 [63] and converted into a tetrahedral volume mesh, ready to be employed for our subsequent simulations.

Since the final cell geometry is newly designed and not found in the literature, appropriate model parameters are not available a priori and need to be properly defined. To avoid unnecessary complication, we reuse all previously specified model parameters from Appendix A. In so doing, the total capacity of the anode falls below the one of the cathode by about 25.4% based on the cell geometry, and the anode thus becomes the limiting electrode defining the state of charge of the entire cell. The temperature throughout the computational domain is set to 298 K without exception, so that the Arrhenius relation (A.1), the associated activation energies from Table A.7, and the resulting Arrhenius plots from Figure A.28 are no longer relevant. We perform adaptive numerical time integration in exactly the same way as before, albeit with the larger values 25 s and 5 s of the main and reduced time step sizes, respectively.

The simulation considered in the following involves lithium plating and stripping due to overcharging and covers a full cycle consisting of a galvanostatic charge process at a charge rate of 0.02 C until an upper cutoff voltage of 4.2 V, a relaxation phase with a duration of 30 s, and a galvanostatic discharge process at a discharge rate of again 0.02 C down to a lower cutoff voltage of 3 V. While the charge and discharge rates are, in absolute terms, much smaller than the ones applied to our first cell from Section 4.1, we point out that lithium plating and stripping as well as their electrochemical interaction with lithium intercalation and deintercalation are rather affected by the magnitudes of the intercalation and plating currents at the anode-electrolyte interface. These magnitudes are still smaller than before, but not by quite as much as the charge and discharge rates, given that the electrode particles are now overall much larger, and the surface-to-volume ratio is lower accordingly. More precisely, the present value of 0.02 C corresponds to a value of approximately 0.28 C in the previous problem setup under the assumption of an identical, spatially averaged total electric current density at the anode-electrolyte interface. Picking this comparatively small number provides insight into a physical mechanism unnoticed so far, as will be discussed in the next section.

4.2.1. Charge and discharge behavior in the presence of lithium plating and stripping

We first consider the influence of lithium plating and stripping on the charge and discharge behavior of the cell. The set of simulation results presented in Figure 22 is of the same kind as the one from Figure 19 apart from the reduced number of half cycles captured by the present simulation. To prevent the diagram in the left panel from being horizontally distorted, we treat plated lithium as intercalated lithium when computing the state of charge of the cell based on the state of charge of the anode as the limiting electrode. Since the small charge rate leads to a rather quasistatic charge behavior exhibiting only minor interfacial overpotentials and shallow spatial gradients of the electric or electrochemical potential inside the cell, the simulation results differ from the previous ones in several respects: Firstly, lithium plating already starts
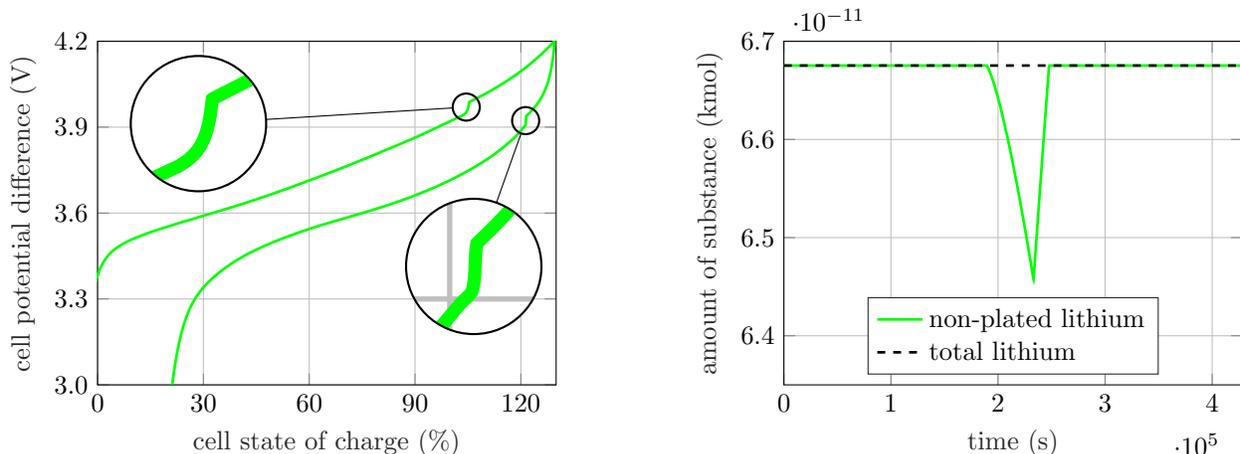
Figure 22: Cell potential difference (left) and amounts of non-plated and total lithium (right) during one full cycle.

at a much lower threshold of the overall cell potential difference around $4\,\mathrm{V}$ during the charge process, as indicated by the usual, magnified kink along the upper branch of the curve in the left panel at approximately 105.3% state of charge of the cell. Secondly, the downward jump in the overall cell potential difference due to the reversal of the overall electric current from charge to discharge is less pronounced, i.e., the vertical curve segment in the left panel at the maximum state of charge of the cell is shorter and hardly recognizable at all. And thirdly, we found that the maximum local film thickness of plated lithium at the end of the charge process is larger than before by far more than one order of magnitude in spite of the smaller upper cutoff voltage, as confirmed by the much greater relative depth of the localized, downward spike in the right panel, i.e., by the much greater portion of lithium contributing to lithium plating. More specifically, the local film thickness of plated lithium peaks at around $60\,\mathrm{nm}$ in the current simulation, whereas the maximum value reached across all simulations from Section 4.1.2 is approximately $1\,\mathrm{nm}$ in the $9\,\mathrm{C}$ simulation from Figures 9 and 10. Again, the dashed, black line in the right panel remains exactly horizontal throughout the simulation as expected, and the amounts of non-plated and total lithium deviate from each other only within the interval covered by the spike, underlining the accuracy of our modeling and simulation approach.

Unlike before, we now identify a pronounced kink also along the lower branch of the curve in the left panel, as highlighted by the second magnifying close-up. This kink marks the final stages of lithium stripping during the discharge process, where the plating current ceases under the control of our novel regularization technique after consuming all plated lithium. The intercalation current and the corresponding interfacial overpotential are elevated at the same time to maintain a constant, spatially averaged total electric current density at the anode-electrolyte interface according to the prescribed discharge rate. Since the electric potential inside the anode is constrained by the homogeneous Dirichlet boundary condition (21) applied to the anode-side current collector, the electrochemical potential inside the electrolyte and the electric potential inside the cathode go down in compliance with the definition (9) of the interfacial overpotential, and we ultimately observe a drop in the overall cell potential difference. In this sense, the kinks along the lower and upper branches of the curve constitute reversed counterparts of each other and, as such, stem from similar mechanisms of interaction between the intercalation and plating currents. Comparable drops in the overall cell potential difference have been detected experimentally in [4, 11, 12, 64–66] and numerically in [6, 29, 67], among other publications.

The fundamental reason why our previous simulations from Section 4.1 do not visibly exhibit this drop in the overall cell potential difference at the end of lithium stripping is that the charge rates chosen earlier are much larger, as are the resulting interfacial overpotentials and spatial gradients of the electric or electrochemical potential inside the cell, and hence the overall cell potential difference. This dynamic charge behavior causes the end of the charge process at the upper cutoff voltage to be reached quickly, i.e., after only a thin lithium film has been deposited at the anode-electrolyte interface. In each simulation from Figures 9
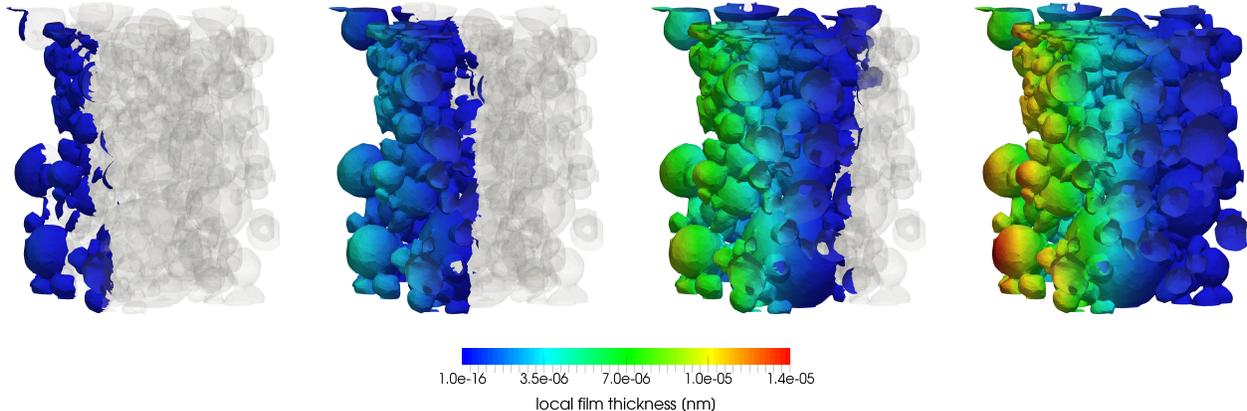
Figure 23: Propagation of plated lithium through the anode at the onset of lithium plating after about 2.2 days of charging.

through 14, the maximum local film thickness of plated lithium is below $d_{\mathrm{reg}} = 0.29\,\mathrm{nm}$ at the beginning of the discharge process, implying that the final stages of lithium stripping are completed either already during the comparatively dynamic relaxation phase or, at the latest, very soon after the beginning of the discharge process, where the corresponding curve is fully or nearly vertical. As a consequence, the drop in the overall cell potential difference merges into the curve and cannot be visually identified. By contrast, the end of lithium stripping occurs later during the discharge process in the present numerical example, i.e., it falls into a flatter curve segment further away from the maximum state of charge of the cell, given that the near-quasistatic charge process builds up a much thicker lithium film and also largely prevents any local intercalation of plated lithium into the anode during the relaxation phase, and the subsequent dissolution of all plated lithium therefore takes significantly longer. In addition, the near-quasistatic charge and discharge processes keep the anode-side lithium concentration at the anode-electrolyte interface at a high level close to $c_{\mathrm{ed,max}}$ during lithium stripping, so that i_0^{int} is small according to its definition (8) and, at the same time, the associated interfacial overpotential remains negative, albeit to a lesser extent than during the preceding charge process, due to some marginal local intercalation of plated lithium into the anode. It follows from the Butler–Volmer charge transfer kinetics (7) that a substantial growth in the interfacial overpotential is required to ramp up the intercalation current as soon as lithium stripping ceases, leading to a pronounced drop in the overall cell potential difference. By comparison, the much larger charge rate from each of our previous simulations induces rather steep spatial gradients of the lithium concentration inside the anode. Since these spatial gradients are reduced during the relaxation phase, the anode-side lithium concentration at the anode-electrolyte interface is no longer close to $c_{\mathrm{ed,max}}$ at the end of lithium stripping, and we obtain a large i_0^{int} and only a mild increase in the interfacial overpotential. The drop in the overall cell potential difference thus becomes small and even more undetectable.

4.2.2. Spatially inhomogeneous propagation of plated lithium through the anode microstructure

Having investigated the global charge and discharge behavior of the cell in the presence of lithium plating and stripping, we now turn our attention to the onset of lithium plating, focusing on the percolation of plated lithium through the entire anode microstructure. The four snapshots presented in Figure 23 were taken in quick succession during the initial emergence of plated lithium after approximately 2.2 days of charging. Each snapshot captures only the anode of the cell from the same perspective as in Figure 21, i.e., we need to imagine the cathode to be positioned to the left of the anode. The color bar specifies the spatial distribution of the local film thickness of plated lithium throughout the anode-electrolyte interface and equally applies to all four snapshots. To prevent regions of the anode-electrolyte interface without any plated lithium from being colored, the lower bound of the color bar is set to the value 10^{-16} close to double-precision machine epsilon rather than to exactly zero. As expected, we deduce from the four snapshots that plated lithium is first deposited at the cathode-side end of the anode and then gradually propagates through the anode before
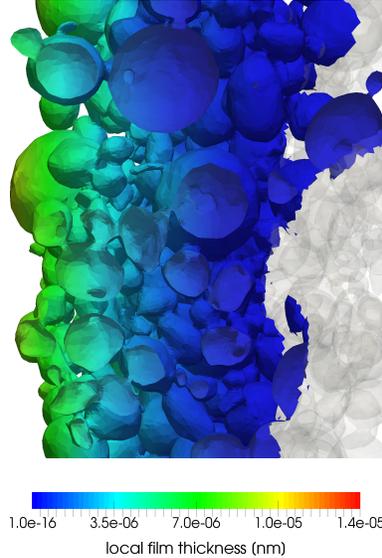
Figure 24: Spatially inhomogeneous percolation of plated lithium in top view of third snapshot from Figure 23.

covering it completely. Owing to the model parameters chosen for the simulation, particularly the very small charge and discharge rates in combination with the relatively high ionic conductivity of the electrolyte, the first and last snapshots are only less than one second apart from each other, see also our previous discussion from Section 4.1.5. In reverse order, the four snapshots also describe the temporal evolution of the local film thickness at the end of lithium stripping, though the regions of the anode-electrolyte interface with and without plated lithium are not as clearly separable due to the spatial smearing introduced by our novel regularization technique.

A closer look especially at the third snapshot reveals that the penetration of plated lithium through the anode is spatially inhomogeneous in that the axial intrusion depth differs from region to region. Clearer evidence of this phenomenon is offered by Figure 24, where a more detailed top view of the third snapshot is provided. We observe that the lithium film already touches the anode-side current collector in a locally confined area while being behind in axial direction everywhere else. Building on our previous discussion from Section 4.1.5, we may generally state that the anode-electrolyte interface is more susceptible to lithium plating wherever it is better accessible to the lithium ions inside the electrolyte. More precisely, a shorter overall percolation path of a lithium ion arriving at the anode-electrolyte interface during the charge process results in a smaller drop in the electrochemical potential inside the electrolyte along the way, and hence in a larger electrochemical potential at the anode-electrolyte interface. As a consequence, the interfacial overpotential pertaining to the plating current falls below zero faster and lithium plating starts earlier, so that the lithium film built up until the end of the charge process is more pronounced. An analogous argument can be made for the electrons traveling through the anode, albeit to a lesser extent due to the relatively high electronic conductivity inside the anode and the correspondingly minor spatial gradients of the electric potential. We found that this line of reasoning is indeed reflected in the simulation results underlying the third snapshot, and we conclude that the stochastic nature of the sizes and positions of the anode particles inevitably provokes spatial variations in the permeability of the anode microstructure to lithium ions and electrons, and hence also in the local film thickness and axial intrusion depth of plated lithium. In fact, a geometric analysis of the anode microstructure confirms that some voids inside the anode microstructure are rather exposed to lithium ions departing from the cathode, whereas others at comparable axial positions are hidden behind clusters of anode particles and can thus only be reached after long detours. Similarly, some anode particles are more straightly chained to the anode-side current collector via contiguous anode particles than others, and the respective distances traveled by the electrons inside the anode therefore diverge.

28

The insight from the preceding paragraph is indicative of a core benefit of our modeling and simulation approach to spatially resolved lithium plating and stripping, given that alternative approaches based on one-dimensional porous electrode theory or equivalent circuit theory are not readily capable of capturing three-dimensional, local effects arising from microstructural inhomogeneities, as discussed in Section 1. Such effects are already very apparent in the present numerical example, although the cell is not overly large and exhibits statistically isotropic electrode microstructures composed of nearly spherical particles with stochastically distributed sizes and positions. Accordingly, lithium plating and stripping are expected to display an even more spatially inhomogeneous behavior in cells with greater dimensions or geometrically biased electrode microstructures, where the additional accuracy offered by the spatial resolution of our approach may become pivotal to reliable, predictive simulation results.

4.2.3. Evolution of the lithium concentration fields inside both electrodes during lithium plating and stripping

Next, we examine the temporal evolution of the lithium concentration fields inside both electrodes within the time period where lithium plating and stripping occur. The three snapshots in Figure 25 were taken from the same perspective as Figure 21 and capture, from top to bottom, the onset of lithium plating, the end of the charge process, and the end of lithium stripping after respective timespans of approximately 2.2, 2.7, and 2.9 days since the start of the simulation. With reference to the left panel of Figure 22, the first snapshot corresponds to the kink along the upper branch of the curve, the second one to the reversal point in the top right corner, and the third one to the kink along the lower branch of the curve. The coloring of each snapshot specifies the lithium concentration fields inside the cathode on the left and the anode on the right according to the common color bar at the bottom. The lithium concentration fields at the beginning of the discharge process do not visually differ from the ones at the end of the charge process due to the comparatively short duration of the relaxation phase and the low charge rate. In quantitative terms, the lithium concentration values inside both electrodes vary only in the third significant figure throughout the relaxation phase.

Focusing on the cathode first, we observe that lithium deintercalation during the charge process gradually depletes the lithium concentration at the cathode-electrolyte interface and thus propagates spatial gradients of the lithium concentration into the interior of the cathode. At the end of the charge process, the lithium concentration at the cathode-electrolyte interface reaches its overall minimum, while the lithium concentration in the interior of the cathode is noticeably higher. Since the relaxation phase between the charge and discharge processes is too short to have a visible effect on the non-equilibrated lithium concentration field, the actual relaxation of the spatial gradients therein extends far into the discharge process up until the end of the simulation, as implied by the apparent decay of the red color from the second snapshot to the third one. Given that lithium intercalation during the discharge process causes the lithium concentration at the cathode-electrolyte interface to rise again, we obtain radially non-monotonic lithium distributions exhibiting opposite spatial gradients especially inside big cathode particles with high electrochemical inertia, i.e., the lithium concentration is larger in the centers and towards the outer surfaces of the particles than in between.

Moving on to the anode, we deduce from the snapshots that the lithium concentration at the anode-electrolyte interface remains at an almost constant level close to $c_{\mathrm{ed,max}}$ from Table A.3 throughout the covered time period between the onset of lithium plating and the end of lithium stripping, see also our previous discussion from Section 4.2.1. The interfacial exchange current density (8) associated with the intercalation current inherently prevents the lithium concentration at the anode-electrolyte interface from surpassing $c_{\mathrm{ed,max}}$, so that excess lithium ions arriving at the anode-electrolyte interface during the charge process are deposited as plated lithium on the anode surface. One can thus imagine the anode to be shielded from lithium intercalation by the lithium film and hence, in a way, to be decoupled and isolated from the electrolyte and the cathode. Compared to the spatial gradients of the lithium concentration inside the cathode, the ones inside the anode are naturally reversed, but otherwise qualitatively identical, and the corresponding insight gained for the cathode in the preceding paragraph therefore analogously applies to the anode as well.
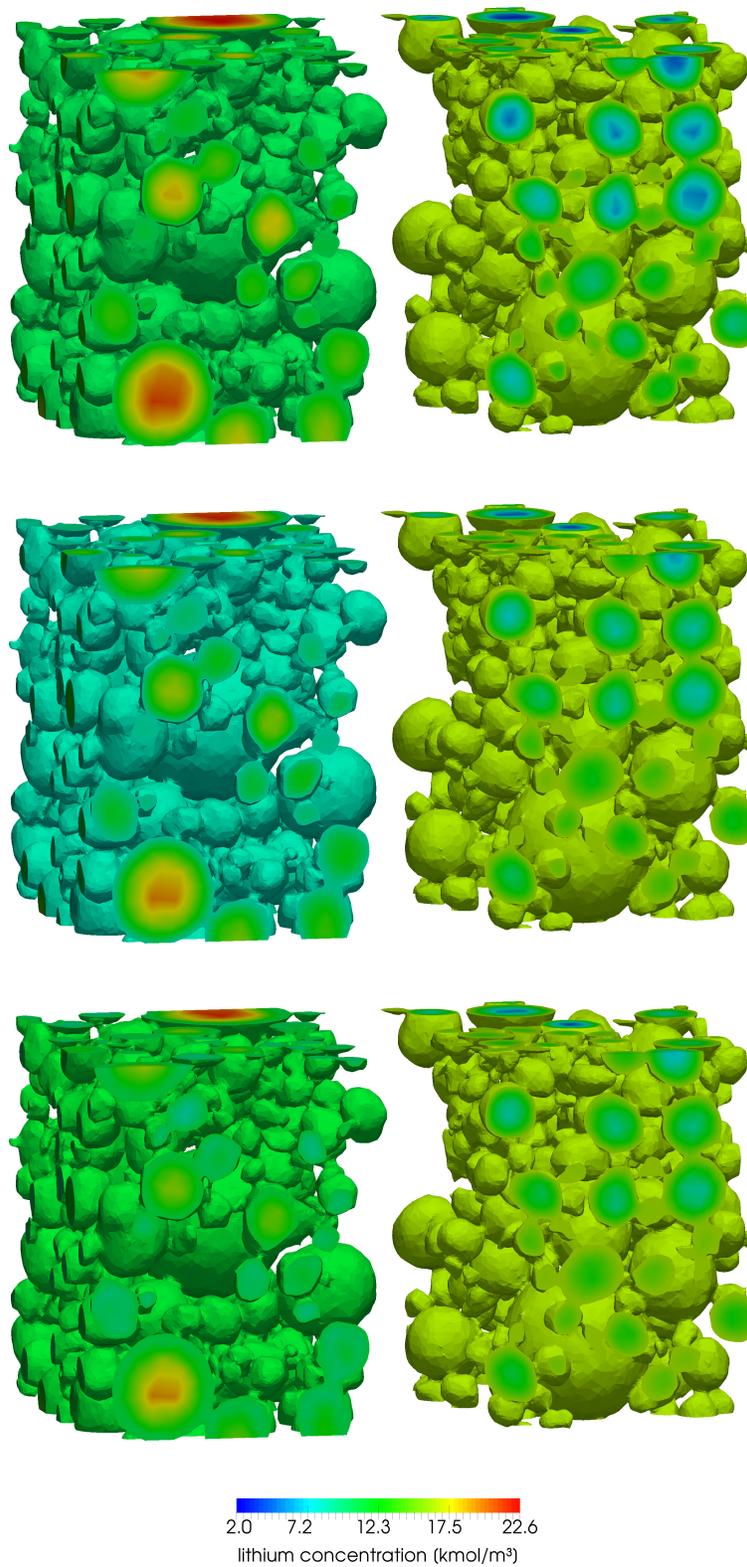
Figure 25: Lithium concentration fields inside the cathode (left) and anode (right) at the onset of lithium plating (top), at the end of the charge process (middle), and at the end of lithium stripping (bottom) after about 2.2, 2.7, and 2.9 days, respectively.
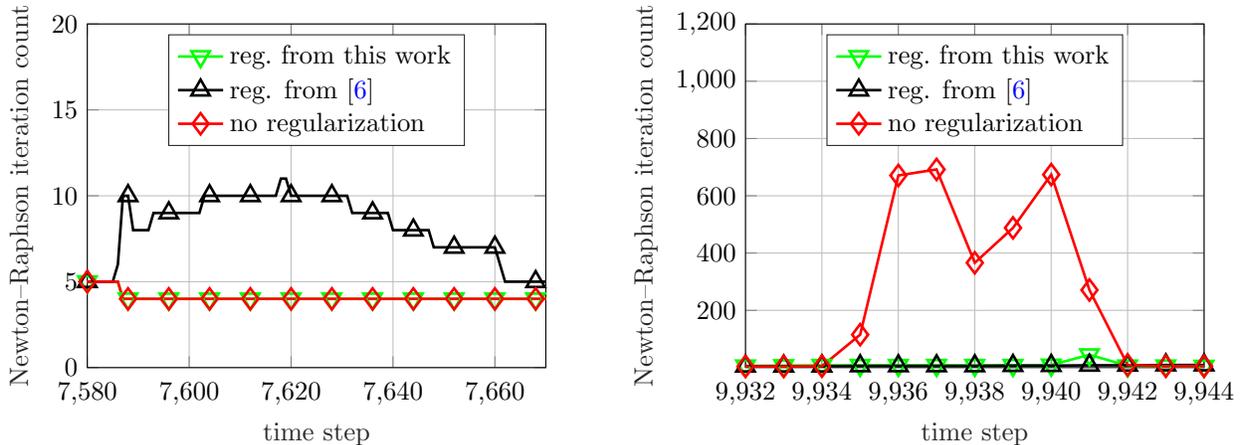
Figure 26: Newton–Raphson iteration counts at the onset of lithium plating (left) and at the end of lithium stripping (right).

4.2.4. Effect of regularization on the convergence behavior of the Newton–Raphson method

Lastly, we examine the impact of regularization on the convergence properties of the Newton–Raphson method, thereby exposing the general necessity of regularization as well as the practical applicability of our novel regularization technique. For this purpose, we perform two reruns of the present simulation, replacing our regularization with $d_{\mathrm{reg}} = 0.29\,\mathrm{nm}$ by the one from [6] with $d_{\mathrm{reg}} = 0.48\,\mathrm{nm}$ in the first rerun and employing no regularization at all in the second rerun, as done before in Section 4.1.7.

The convergence behavior of the Newton–Raphson method in all three simulations is visualized and compared in Figure 26, where the Newton–Raphson iteration counts at the beginning of lithium plating and at the end of lithium stripping are plotted as a function of the time step in the left and right panels, respectively. Focusing on the beginning of lithium plating first, we recall that either of the two function graphs from Figures 2 and 4 exhibits a kink at the origin of the coordinate system. As a consequence, we obtain a locally semi-smooth Newton–Raphson method involving only C^0 continuity and hence discontinuous linearizations. The diagram in the left panel reveals that the two associated simulations still achieve convergence within as few as 4 to 5 Newton–Raphson iteration steps from the time step 7,586 onward, where lithium plating is initiated. The smoothness of the function graph from Figure 3, on the other hand, is worse due to the jump at the origin of the coordinate system, and roughly twice as many Newton–Raphson iteration steps are required for convergence accordingly. However, we point out that the regularization from [6] is not necessarily expected to work well at the beginning of lithium plating, since the goals of the authors are different from ours, and they therefore do not actually investigate the beginning of lithium plating in their simulations. In our understanding, they only identify the point where the plating condition is satisfied, i.e., where the interfacial overpotential pertaining to the plating current becomes negative, without evaluating the plating current and growing a corresponding lithium film. Besides, the authors also study lithium stripping in the presence of plated lithium, starting from positive local film thickness values already fulfilling the plating condition. As a result, the regularization from [6] is primarily designed for lithium stripping instead of lithium plating, and the convergence issues of the Newton–Raphson method at the beginning of lithium plating are thus left unaddressed in the publication.

Moving on to the right panel characterizing the end of lithium stripping, we observe that hundreds of Newton–Raphson iteration steps are required for convergence in several consecutive time steps during the simulation without any regularization. As expected based on our analysis of Figure 2, these time steps exactly coincide with the challenging simulation phase where the deposited lithium film retreats from the anode surface and covers it only partially, so that the local film thickness of plated lithium just reaches zero in some regions of the anode surface. In a series of numerical experiments, we found out that the severeness of the disturbances to the convergence of the Newton–Raphson method is qualitatively correlated
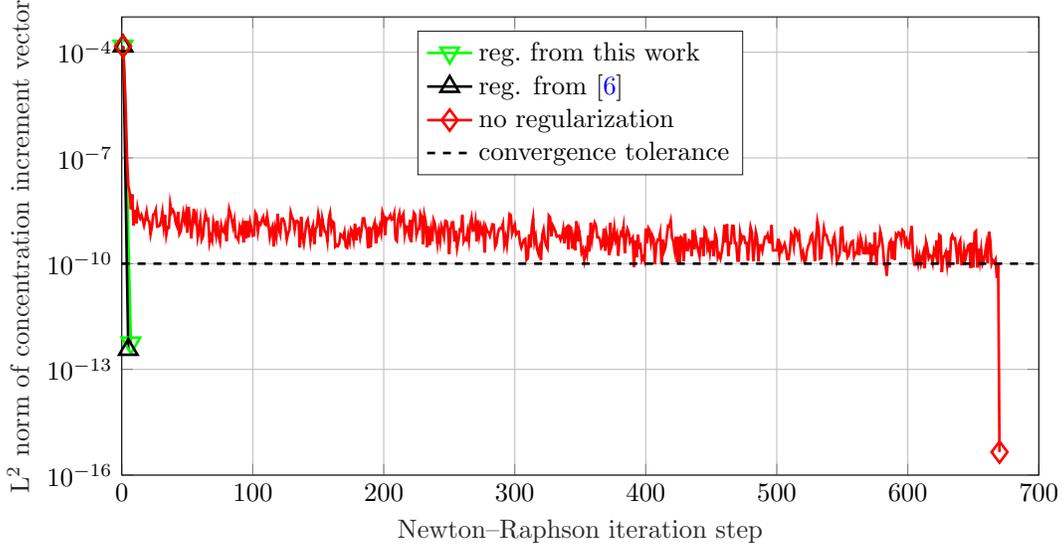
31

Figure 27: Convergence behavior of the overall lithium concentration field inside the entire cell at the time step 9,936.

with the amplitude of the drop in the overall cell potential difference at the end of lithium stripping, see also Section 4.2.1. The two other simulations, by contrast, do not produce any noticeably increased Newton–Raphson iteration counts in the diagram apart from a very slight deflection in the green curve associated with our novel regularization technique at the time step 9,941. The regularization from [6] does not exhibit this deflection, since it heavily smears the non-regularized function graph from Figure 2, thereby significantly decelerating and prematurely stalling lithium stripping according to our discussion from Section 4.1.7. As a consequence, the deposited lithium film is not completely dissolved throughout the discharge process, and we never reach the critical moment at the end of lithium stripping where the local film thickness of plated lithium approaches zero. We conclude that the regularization from [6] is inherently forgiving and not prone to convergence issues during lithium stripping, at the cost of being considerably less accurate in physical terms.

The increased Newton–Raphson iteration counts recorded in the left and right panels of Figure 26 agree with our previous findings from Section 4.1.7 and are qualitatively observed also in the other simulations from Section 4.1 after replacing our novel regularization technique by the regularization from [6] or no regularization at all. However, the severeness of the convergence issues is more pronounced in the present problem setup especially at the end of lithium stripping, as is the resulting necessity for reliable and effective regularization. For instance, each of the time steps involving close to 700 Newton–Raphson iteration steps according to the diagram in the right panel takes around ten hours until convergence despite the large number of CPUs allocated in parallel on our high-performance computer cluster. Our novel regularization technique offers a crucial improvement in computational efficiency by significantly cutting down the required run time, and the saving can be further enhanced if needed in certain scenarios by simply increasing the underlying regularization length. In so doing, the discontinuity removal provided by our regularization extends to a larger number of time steps and thus poses an even smaller numerical challenge to the Newton–Raphson method. Furthermore, we confirmed based on the simulation results that our regularization is minimally intrusive by construction, since it remains inactive throughout the charge process, the relaxation phase, and the beginning of the discharge process. Correspondingly, the simulations employing our regularization and no regularization at all yield exactly identical simulation results, including Newton–Raphson iteration counts, until reaching the time step 9,928 shortly before the time step interval covered by the diagram in the right panel. At this point, lithium stripping has locally reduced the lithium film to a thickness below $d_{\mathrm{reg}} = 0.29\,\mathrm{nm}$ for the first time, so that our regularization is switched on and starts to alter the simulation results.

32

Figure 27 further analyzes the convergence behavior of the Newton–Raphson method at the time step 9,936, where close to 700 Newton-Raphson iteration steps are detected for the first time during the simulation without any regularization. The diagram similarly applies to the subsequent time steps during the critical simulation phase as well. More specifically, the relative L^2 norm of the discrete solution increment vector pertaining to the overall lithium concentration field inside the entire cell is logarithmically plotted as a function of the Newton–Raphson iteration step. The convergence of the electric or electrochemical potential behaves in a qualitatively identical way and is therefore not visualized in the diagram, while the convergence tolerance of 10^{-10} defined in Section 2.5 is indicated by the dashed, black line. Whereas the two simulations involving regularization converge rapidly and monotonically within very few Newton–Raphson iteration steps, the simulation without any regularization soon enters a sustained convergence plateau exhibiting a stagnation of the relative L^2 norm far away from machine epsilon in the presence of slight, continuous oscillations. Although the lower amplitudes of these oscillations occasionally fall below the convergence tolerance in the course of the convergence plateau, we do not obtain comprehensive convergence already at an earlier point because of the electric or electrochemical potential. In the very last Newton–Raphson iteration step at the end of the convergence plateau, the relative L^2 norm abruptly shoots downwards by several orders of magnitude and instantaneously reaches a value near machine epsilon. Convergence of both the lithium concentration and the electric or electrochemical potential is thus eventually achieved, but it occurs rather randomly and unexpectedly, implying that the Newton-Raphson method severely lacks computational robustness.

In this light, we also observed in a series of numerical experiments that the Newton–Raphson iteration counts are highly sensitive to all major characteristics of the problem setup. For example, the geometry and meshing of the cell determine the number of degrees of freedom associated with lithium plating and stripping relative to the total number of degrees of freedom. The larger this ratio is, the more challenging the problem tends to be due to a stronger necessity for effective regularization. In addition, the model parameters from Appendix A play an important role, as do the operating conditions such as the temperature, the charge and discharge rates, the lower and upper cutoff voltages, and the duration of the relaxation phase. Another factor of influence is given by numerical settings, including the convergence tolerances chosen for the Newton–Raphson method and the iterative linear solver, the regularization length, and parallelization aspects, i.e., the number of allocated CPUs and the partitioning of the problem across all CPUs. And lastly, algorithmic features have an impact on the resulting Newton–Raphson iteration counts as well. For instance, our monolithic Newton–Raphson scheme converges within finite Newton–Raphson iteration counts in all time steps even without any regularization, whereas a partitioned Newton–Raphson scheme exhibiting less computational robustness is expected to perform much worse. The time integration scheme, its adaptiveness, and the underlying time step sizes constitute further relevant input variables, and we finally found both in this work and in our previous work from [52] that less powerful linear solvers generally induce greater Newton–Raphson iteration counts, if not divergence.

All in all, our experience definitely shows that the Newton–Raphson method is, by no means, guaranteed to converge and may very well even diverge in simulations involving the regularization from [6] or no regularization at all, especially upon reaching the respective weak points at the beginning of lithium plating and at the end of lithium stripping. Effective and universal regularization, on the other hand, prevents the simulations from requiring prohibitively long run times or from crashing altogether and is thus absolutely necessary in many instances. Our novel regularization technique outperforms the one from [6] overall and offers one feasible way of supporting the Newton–Raphson method in achieving convergence robustly and quickly throughout all simulation phases. The intensity of our regularization increases with the regularization length, albeit at the cost of more artificial smearing and hence less physical accuracy.

5. Conclusion

The principal objective of this work is to present a coupled finite element approach to spatially resolved lithium plating and stripping in three-dimensional anode microstructures of lithium-ion cells. The proposed approach can be consistently incorporated into existing simulation frameworks for lithium-ion cells and

offers the possibility of capturing lithium plating and stripping during cell cycling in one single simulation without any interruptions. Accurate, in-depth, and predictive numerical investigations of lithium plating and stripping are thus enabled as a viable alternative to experimental studies involving sophisticated machinery in most instances.

After establishing the conservation equations for lithium mass and electric charge as well as the associated interface, boundary, and initial conditions, we performed discretization in time and space, treating the local film thickness of plated lithium as an additional primary variable besides the lithium concentrations and the electric or electrochemical potentials inside the electrode and electrolyte phases. The electric resistance of plated lithium is taken into account by the Butler–Volmer charge transfer kinetics governing the intercalation and plating currents, and adaptive numerical time stepping is applied where needed to ensure a good temporal resolution of critical simulation periods. We transformed the resulting discrete system of nonlinear equations into a monolithic system of linear equations by consistently linearizing all discrete residual vectors with respect to all discrete solution vectors according to the iterative Newton–Raphson method chosen as the nonlinear solver. To remove the inherent discontinuity in the plating current and to thus improve the convergence behavior of the Newton–Raphson method, we introduced a novel regularization technique based on a trigonometrical regularization function. We deduced from theoretical considerations that our regularization is superior to the existing one originally proposed in [6] in that it is physically more justified, mathematically more favorable, and conceptually less intrusive due to its local confinement. In particular, our regularization allows an already deposited lithium film to be completely dissolved without prematurely stalling lithium stripping, and we obtain a physical interpretation of our regularization function by setting the regularization length to the thickness of a lithium monolayer, i.e., to the diameter of a lithium atom. Our decision to solve all governing equations in a monolithic, implicit fashion is motivated by achieving better computational robustness and efficiency as compared to partitioned solution schemes, and we adopt the advanced, physics-oriented preconditioning and solution approach from [52] to counter the naturally bad conditioning of the system.

In our numerical examples, we extensively studied two different lithium-ion cells, one with academic electrode microstructures composed of ideally spherical particles, and another one with realistic electrode microstructures gained from X-ray tomography data. The total numbers of degrees of freedom amount to approximately 300,000 and 2.3 million, respectively, proving the practical applicability of our modeling and simulation approach to large and complex problem setups. We successfully validated our basic finite element implementation with the help of simulation results from the literature, and we demonstrated that our approach is physically plausible and sensitive to all three major causes of lithium plating, namely overcharging, fast charging, and low-temperature charging. Among other things, we examined the impact of the operating conditions, the relaxation time, and the ionic conductivity of the electrolyte on lithium plating and stripping. The peculiarities in the behavior of the overall cell potential difference at the beginning of lithium plating and at the end of lithium stripping were thoroughly discussed. We detected and explained significant spatial inhomogeneities in the propagation of plated lithium through the anode microstructure, thereby revealing a core benefit of the spatial resolution provided by our approach, but not by simplified alternatives based on geometric homogenization via morphological model parameters. Moreover, we investigated the temporal evolution of the lithium concentration fields inside both electrodes during lithium plating and stripping, realizing that the lithium film deposited during lithium plating somewhat shields the anode from the intercalation current and thus decouples it from the electrolyte and the cathode. Also, the relaxation of spatial gradients of the lithium concentration was clearly observable especially inside large electrode particles. By directly comparing simulations involving our novel regularization technique, the existing one from [6], and no regularization at all, we confirmed that our regularization very effectively supports the Newton–Raphson method in achieving convergence robustly and quickly at the end of lithium stripping, whereas the regularization from [6] shows increased Newton–Raphson iteration counts at the beginning of lithium plating and, above all, can deliver physically inaccurate simulation results as predicted. Since the high Newton–Raphson iteration counts recorded for the regularization from [6] and for no regularization at all strongly depend on the geometry and meshing of the cell, the model parameters and operating conditions, and the numerical settings and algorithmic features of the solution scheme, the Newton–Raphson method is not guaranteed to

Table A.1: Model parameters for anode and cathode [58].

Parameter	D_{ed}	σ_{ed}	$c_{\mathrm{ed}}^{0\%}$	$c_{\mathrm{ed}}^{100\%}$	c_{ed}^{0}
Unit	$\mathrm{m^2\,s^{-1}}$	$\mathrm{S\,m^{-1}}$	$\mathrm{kmol\,m^{-3}}$	$\mathrm{kmol\,m^{-3}}$	$\mathrm{kmol\,m^{-3}}$
Anode	2.0×10^{-16}	100.0	2.029	10.88	2.029
Cathode	3.7×10^{-16}	10.0	22.37	10.56	22.37

Table A.2: Model parameters for electrolyte [58].

Parameter	D_{el}	t_{el}	f_{el}	A_{el}	k_{el}	d_{el}	c_{el}^{0}
Unit	$\mathrm{m^2\,s^{-1}}$	$-$	$-$	$\mathrm{S\,m^2\,kmol^{-1}}$	$\mathrm{m^{4.2}\,kmol^{-1.4}}$	$-$	$\mathrm{kmol\,m^{-3}}$
Electrolyte	2.6×10^{-10}	0.363	1.0	1.58	0.85	1.4	1.2

converge and may even diverge in the corresponding simulations. Therefore, the advantages offered by our regularization become imperative to prevent prohibitively long run times and simulation aborts.

As a brief outlook for future work, we suggest the following research topics: Firstly, our modeling and simulation approach may be enriched by supplementary functionality taking account of the irreversibility of lithium plating and stripping due to aging and degradation mechanisms [7, 37, 68, 69]. These include the formation and gradual, continuous growth of a solid-electrolyte interphase consuming mobile lithium and increasing the electric resistance at the anode-electrolyte interface in addition to lithium plating, see, e.g., [9, 12, 70, 71] for experimental evidence thereof. The capability of our approach to capture lithium plating and stripping during cell cycling in one single simulation without any interruptions naturally facilitates the incorporation of irreversible effects potentially interacting with lithium plating and stripping in a concurrent, localized, spatially inhomogeneous manner. Secondly, we may represent the lithium film built up during lithium plating by another three-dimensional, spatially resolved phase besides the existing electrode and electrolyte phases instead of merely computing a separate primary variable associated with the local film thickness of plated lithium. In so doing, even thick lithium films resulting from prolonged lithium plating and potentially leading to stochastic dendrite growth may be accurately simulated. This allows us to study further electrochemical phenomena arising from the morphological impact of plated lithium on the electrode and electrolyte phases. For instance, we may observe self-accelerated lithium plating at the protruding tips of dendrites, where lithium plating is favored due to the comparatively short distance to the cathode and the correspondingly small interfacial overpotential associated with the plating current. Thirdly, we may apply our approach to non-isothermal lithium-ion cells with spatially varying temperature fields inside the electrode and electrolyte phases and at the respective boundaries. Moreover, the consideration of electrochemical double layers and their influence on lithium plating and stripping constitutes another research direction [72, 73]. And lastly, our work may be extended towards the modeling and simulation of redox shuttles, i.e., electrolyte additives yielding intrinsic overcharge protection [74].

Appendix A. Model parameters

Tables A.1 through A.4 provide the model parameters and initial conditions adopted from [48, 58] for our simulations. The model parameters were originally determined for the so-called FreedomCAR cell [44, 58] composed of a graphite anode and an NCA cathode, and they do not take account of lithium plating and stripping. Therefore, additional model parameters characterizing lithium plating and stripping are

Table A.3: Model parameters for lithium intercalation and deintercalation at electrode-electrolyte interfaces [58].

Parameter	$\alpha_{\mathrm{a}}^{\mathrm{int}}$	$\alpha_{\mathrm{c}}^{\mathrm{int}}$	k^{int}	$c_{\mathrm{ed,max}}$
Unit	–	–	$\mathrm{m}^{2.5}\,\mathrm{kmol}^{-0.5}\,\mathrm{s}^{-1}$	$\mathrm{kmol\,m}^{-3}$
Anode-electrolyte interface	0.5	0.5	4.52×10^{-8}	16.1
Cathode-electrolyte interface	0.5	0.5	2.07×10^{-8}	23.9

Table A.4: Redlich–Kister expansion coefficients for electrode-electrolyte interfaces [48, 58].

Coefficient $\left(\mathrm{J\,kmol}^{-1}\right)$	Anode-electrolyte interface	Cathode-electrolyte interface
ΔG	1.1652×10^7	3.954616×10^8
A_0	-3.268×10^6	-7.676×10^7
A_1	3.955×10^6	3.799×10^7
A_2	-4.573×10^6	-2.873×10^7
A_3	6.147×10^6	1.169×10^7
A_4	-3.339×10^6	1.451×10^7
A_5	1.117×10^7	-8.938×10^7
A_6	2.997×10^5	1.671×10^8
A_7	-4.866×10^7	-7.236×10^7
A_8	1.362×10^5	-1.746×10^8
A_9	1.373×10^8	-4.067×10^8
A_{10}	-2.129×10^7	9.534×10^8
A_{11}	-1.722×10^8	5.897×10^8
A_{12}	3.956×10^7	-7.455×10^8
A_{13}	9.302×10^7	-1.102×10^9
A_{14}	-3.280×10^7	-2.927×10^8
A_{15}	0.0	7.214×10^8
A_{16}	0.0	9.029×10^8
A_{17}	0.0	-1.599×10^8
A_{18}	0.0	6.658×10^8
A_{19}	0.0	-1.084×10^9

Table A.5: Model parameters for lithium plating and stripping at anode-electrolyte interface [36].

Parameter	$\alpha_{\mathrm{a}}^{\mathrm{pl}}$	$\alpha_{\mathrm{c}}^{\mathrm{pl}}$	k^{pl}
Unit	–	–	$\mathrm{kmol}^{0.7}\,\mathrm{m}^{-1.1}\,\mathrm{s}^{-1}$
Anode-electrolyte interface	0.3	0.7	1.77×10^{-9}

Table A.6: Material properties of lithium.

Parameter	σ_{Li}	M_{Li}	ρ_{Li}
Unit	$\mathrm{S\,m}^{-1}$	$\mathrm{kg\,kmol}^{-1}$	$\mathrm{kg\,m}^{-3}$
Lithium	1.06×10^7	6.941	5.34×10^2

Table A.7: Activation energies relevant to Arrhenius relation (A.1).

Activation energy $\left(\mathrm{J\,kmol^{-1}}\right)$	$E_{D_{\mathrm{ed}}}$	$E_{k^{\mathrm{int}}}$	$E_{k^{\mathrm{pl}}}$
Anode or anode-electrolyte interface	5.31×10^7 [76]	6.8×10^7 [75]	3.53×10^7 [36]
Cathode or cathode-electrolyte interface	5.31×10^7 *	4.9×10^7 [75]	–

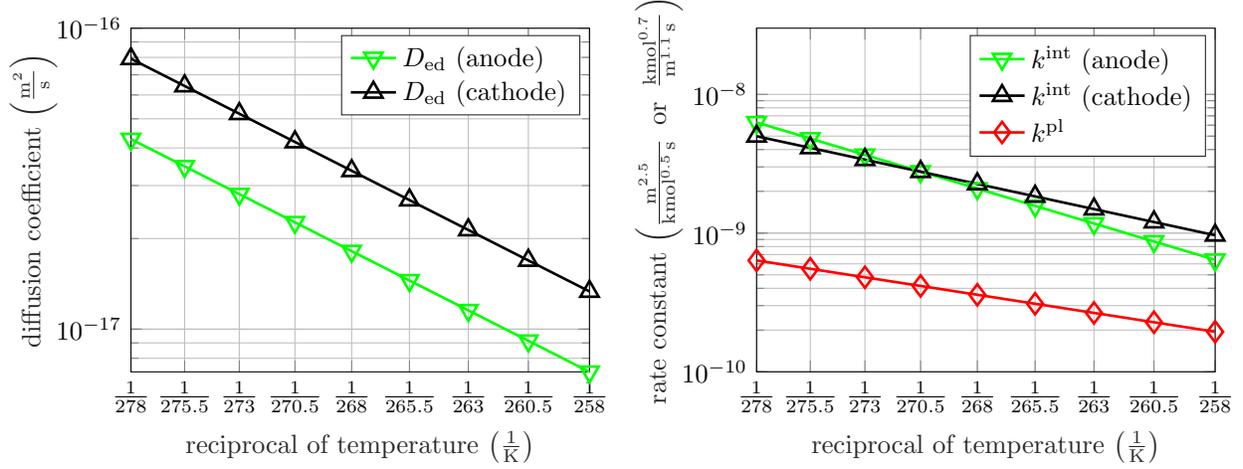* assumed value due to lack of literature data

Figure A.28: Arrhenius plots displaying temperature dependencies of diffusion coefficients (left) and rate constants (right).

extracted from [36] and listed in Table A.5. Besides, commonly known material properties of lithium can be found in Table A.6. We remark that the initial lithium concentrations inside both electrodes are set to the respective average lithium concentrations at 0% state of charge according to Table A.1, so that we start with a completely discharged cell.

Unless stated otherwise, we choose the value 298 K for the temperature inside the entire cell, as also done in [36, 58]. In case a different temperature T is considered, we modify the diffusion coefficients from Table A.1 as well as the rate constants from Tables A.3 and A.5 according to the following Arrhenius relation [36]:

$$\chi(T) = \chi(298\,\mathrm{K}) \exp\left(\frac{E_\chi}{R}\left(\frac{1}{298\,\mathrm{K}} - \frac{1}{T}\right)\right). \tag{A.1}$$

Herein, $\chi(298\,\mathrm{K})$ represents the values of D_{ed}, k^{int}, and k^{pl} from Tables A.1, A.3, and A.5, whereas $\chi(T)$ denotes the respective modified values. The corresponding activation energies E_χ are taken from [36, 75, 76], see Table A.7. The resulting temperature dependencies are visualized by the classical Arrhenius plots in Figure A.28, where each of the two diagrams in the left and right panels exhibits an inversely scaled abscissa associated with the temperature as well as a logarithmically scaled ordinate associated with the diffusion coefficients or rate constants. The Arrhenius relation is thus translated into straight lines, whose slopes are controlled by E_χ. The specific temperature values indicated as denominators are directly correlated with the set of temperature-dependent simulation results from Section 4.1.2.

References

[1] B. Scrosati, J. Garche, Lithium batteries: Status, prospects and future, Journal of Power Sources 195 (9) (2010) 2419–2430.

[2] J. Vetter, P. Novák, M. Wagner, C. Veit, K.-C. Möller, J. Besenhard, M. Winter, M. Wohlfahrt-Mehrens, C. Vogler, A. Hammouche, Ageing mechanisms in lithium-ion batteries, Journal of Power Sources 147 (1) (2005) 269–281.

[3] M. Dollé, L. Sannier, B. Beaudoin, M. Trentin, J.-M. Tarascon, Live Scanning Electron Microscope Observations of Dendritic Growth in Lithium/Polymer Cells, Electrochemical and Solid-State Letters 5 (12) (2002) A286–A289.

[4] M. C. Smart, B. V. Ratnakumar, Effects of Electrolyte Composition on Lithium Plating in Lithium-Ion Cells, Journal of The Electrochemical Society 158 (4) (2011) A379–A389.

[5] J.-M. Tarascon, M. Armand, Issues and challenges facing rechargeable lithium batteries, Nature 414 (6861) (2001) 359–367.

[6] S. Hein, A. Latz, Influence of local lithium metal deposition in 3D microstructures on local and global behavior of Lithium-ion batteries, Electrochimica Acta 201 (2016) 354–365.

[7] J. Keil, A. Jossen, Electrochemical Modeling of Linear and Nonlinear Aging of Lithium-Ion Cells, Journal of The Electrochemical Society 167 (11) (2020) 110535.

[8] J. C. Burns, D. A. Stevens, J. R. Dahn, In-Situ Detection of Lithium Plating Using High Precision Coulometry, Journal of The Electrochemical Society 162 (6) (2015) A959–A964.

[9] M. Petzl, M. Kasper, M. A. Danzer, Lithium plating in a commercial lithium-ion battery – A low-temperature aging study, Journal of Power Sources 275 (2015) 799–807.

[10] Y. Zhang, X. Li, L. Su, Z. Li, B. Y. Liaw, J. Zhang, Lithium Plating Detection and Quantification in Li-Ion Cells from Degradation Behaviors, ECS Transactions 75 (23) (2017) 37–50.

[11] Y. Zhang, H. Ge, J. Huang, Z. Li, J. Zhang, A comparative degradation study of commercial lithium-ion cells under low-temperature cycling, RSC Advances 7 (2017) 23157–23163.

[12] M. Petzl, M. A. Danzer, Nondestructive detection, characterization, and quantification of lithium plating in commercial lithium-ion batteries, Journal of Power Sources 254 (2014) 80–87.

[13] L. Gireaud, S. Grugeon, S. Laruelle, B. Yrieix, J.-M. Tarascon, Lithium metal stripping/plating mechanisms studies: A metallurgical approach, Electrochemistry Communications 8 (10) (2006) 1639–1649.

[14] Y. Krämer, C. Birkenmaier, J. Feinauer, A. Hintennach, C. L. Bender, M. Meiler, V. Schmidt, R. E. Dinnebier, T. Schleid, A New Method for Quantitative Marking of Deposited Lithium by Chemical Treatment on Graphite Anodes in Lithium-Ion Cells, Chemistry – A European Journal 21 (16) (2015) 6062–6065.

[15] H. J. Chang, N. M. Trease, A. J. Ilott, D. Zeng, L.-S. Du, A. Jerschow, C. P. Grey, Investigating Li Microstructure Formation on Li Anodes for Lithium Batteries by in Situ ^{6}Li/^{7}Li NMR and SEM, The Journal of Physical Chemistry C 119 (29) (2015) 16443–16451.

[16] K.-H. Chen, K. N. Wood, E. Kazyak, W. S. LePage, A. L. Davis, A. J. Sanchez, N. P. Dasgupta, Dead lithium: mass transport effects on voltage, capacity, and failure of lithium metal anodes, Journal of Materials Chemistry A 5 (2017) 11671–11681.

[17] S. J. Harris, A. Timmons, D. R. Baker, C. Monroe, Direct in situ measurements of Li transport in Li-ion battery negative electrodes, Chemical Physics Letters 485 (4) (2010) 265–274.

[18] F. Ringbeck, C. Rahe, G. Fuchs, D. U. Sauer, Identification of Lithium Plating in Lithium-Ion Batteries by Electrical and Optical Methods, Journal of The Electrochemical Society 167 (9) (2020) 090536.

[19] J. Yamaki, S. Tobishima, K. Hayashi, K. Saito, Y. Nemoto, M. Arakawa, A consideration of the morphology of electrochemically deposited lithium in an organic electrolyte, Journal of Power Sources 74 (2) (1998) 219–227.

[20] R. Bhattacharyya, B. Key, H. Chen, A. S. Best, A. F. Hollenkamp, C. P. Grey, In situ NMR observation of the formation of metallic lithium microstructures in lithium batteries, Nature Materials 9 (6) (2010) 504–510.

[21] J. Wandt, P. Jakes, J. Granwehr, R.-A. Eichel, H. A. Gasteiger, Quantitative and time-resolved detection of lithium plating on graphite anodes in lithium ion batteries, Materials Today 21 (3) (2018) 231–240.

[22] V. Zinth, C. von Lüders, M. Hofmann, J. Hattendorff, I. Buchberger, S. Erhard, J. Rebelo-Kornmeier, A. Jossen, R. Gilles, Lithium plating in lithium-ion batteries at sub-ambient temperatures investigated by in situ neutron diffraction, Journal of Power Sources 271 (2014) 152–159.

[23] D. Miranda, C. Costa, S. Lanceros-Mendez, Lithium ion rechargeable batteries: State of the art and future needs of microscopic theoretical models and simulations, Journal of Electroanalytical Chemistry 739 (2015) 97–110.

[24] N. Legrand, B. Knosp, P. Desprez, F. Lapicque, S. Raël, Physical characterization of the charging process of a Li-ion battery and prediction of Li plating by electrochemical modelling, Journal of Power Sources 245 (2014) 208–216.

[25] P. Arora, M. Doyle, R. E. White, Mathematical Modeling of the Lithium Deposition Overcharge Reaction in Lithium-Ion Batteries Using Carbon-Based Negative Electrodes, Journal of The Electrochemical Society 146 (10) (1999) 3543–3553.

[26] M. Tang, P. Albertus, J. Newman, Two-Dimensional Modeling of Lithium Deposition during Cell Charging, Journal of The Electrochemical Society 156 (5) (2009) A390–A399.

[27] S. Tippmann, D. Walper, L. Balboa, B. Spier, W. G. Bessler, Low-temperature charging of lithium-ion cells part I: Electrochemical modeling and experimental investigation of degradation behavior, Journal of Power Sources 252 (2014) 305–316.

[28] M. Ecker, S. Käbitz, J. Gerschler, D. U. Sauer, Modeling of Lithium Plating in Lithium-Ion Batteries, ECS Meeting Abstracts MA2010-02 (4) (2010) 201.

[29] S. Carelli, W. G. Bessler, Prediction of Reversible Lithium Plating with a Pseudo-3D Lithium-Ion Battery Model, Journal of The Electrochemical Society 167 (10) (2020) 100515.

[30] Z. Wang, Z. Li, J. Huang, J. Zhang, Formation of a Lithium-Plated Reference Electrode in Lithium-Ion Cells: Characterization Using Dynamic Impedance and Simulation Using Electrochemical Model, ECS Transactions 75 (20) (2017) 151–164.

[31] T. F. Fuller, M. Doyle, J. Newman, Simulation and Optimization of the Dual Lithium Ion Insertion Cell, Journal of The Electrochemical Society 141 (1) (1994) 1–10.

[32] J. Newman, K. E. Thomas-Alyea, Electrochemical Systems, 3rd Edition, John Wiley & Sons, 2004.

[33] R. Akolkar, Mathematical model of the dendritic growth during lithium electrodeposition, Journal of Power Sources 232 (2013) 23–28.

[34] C. Monroe, J. Newman, Dendrite Growth in Lithium/Polymer Systems: A Propagation Model for Liquid Electrolytes under Galvanostatic Conditions, Journal of The Electrochemical Society 150 (10) (2003) A1377–A1384.

[35] K. S. N. Vikrant, S. Allu, Modeling of Lithium Nucleation and Plating Kinetics Under Fast Charge Conditions, Journal of The Electrochemical Society 168 (2) (2021) 020536.

[36] H. Ge, T. Aoki, N. Ikeda, S. Suga, T. Isobe, Z. Li, Y. Tabuchi, J. Zhang, Investigating Lithium Plating in Lithium-Ion Batteries at Low Temperatures Using Electrochemical Model with NMR Assisted Parameterization, Journal of The Electrochemical Society 164 (6) (2017) A1050–A1060.

[37] S. Hein, T. Danner, A. Latz, An Electrochemical Model of Lithium Plating and Stripping in Lithium Ion Batteries, ACS Applied Energy Materials 3 (9) (2020) 8519–8531.

[38] J. Wu, V. Srinivasan, J. Xu, C. Y. Wang, Newton–Krylov-Multigrid Algorithms for Battery Simulation, Journal of The Electrochemical Society 149 (10) (2002) A1342–A1348.

[39] J. Wu, J. Xu, Modeling and Simulations for Electrochemical Power Systems, Springer US, Boston, MA, 2002, pp. 365–381.

[40] C. Danowski, V. Gravemeier, L. Yoshihara, W. A. Wall, A monolithic computational approach to thermo-structure interaction, International Journal for Numerical Methods in Engineering 95 (13) (2013) 1053–1078.

[41] M. W. Gee, U. Küttler, W. A. Wall, Truly monolithic algebraic multigrid for fluid-structure interaction, International Journal for Numerical Methods in Engineering 85 (8) (2010) 987–1016.

[42] M. Heil, A. L. Hazel, J. Boyle, Solvers for large-displacement fluid-structure interaction problems: segregated versus monolithic approaches, Computational Mechanics 43 (1) (2008) 91–101.

[43] S. Hein, Modeling of lithium plating in lithium-ion-batteries, Ph.D. thesis, Universität Ulm (2018).

[44] K. Smith, C.-Y. Wang, Solid-state diffusion limitations on pulse operation of a lithium ion cell for hybrid electric vehicles, Journal of Power Sources 161 (1) (2006) 628–639.

[45] A. Ehrl, J. Landesfeind, W. A. Wall, H. A. Gasteiger, Determination of Transport Parameters in Liquid Binary Lithium Ion Battery Electrolytes: I. Diffusion Coefficient, Journal of The Electrochemical Society 164 (4) (2017) A826–A836.

[46] A. Ehrl, J. Landesfeind, W. A. Wall, H. A. Gasteiger, Determination of Transport Parameters in Liquid Binary Electrolytes: Part II. Transference Number, Journal of The Electrochemical Society 164 (12) (2017) A2716–A2731.

[47] J. Landesfeind, A. Ehrl, M. Graf, W. A. Wall, H. A. Gasteiger, Direct Electrochemical Determination of Thermodynamic Factors in Aprotic Binary Electrolytes, Journal of The Electrochemical Society 163 (7) (2016) A1254–A1264.

[48] A. M. Colclasure, R. J. Kee, Thermodynamically consistent modeling of elementary electrochemistry in lithium-ion batteries, Electrochimica Acta 55 (28) (2010) 8960–8973.

[49] T. Hughes, The Finite Element Method: Linear Static and Dynamic Finite Element Analysis, Dover Civil and Mechanical Engineering, Dover Publications, 2000.

[50] O. C. Zienkiewicz, R. L. Taylor, The finite element method for solid and structural mechanics, Elsevier Butterworth–Heinemann, 2005.

[51] R. Fang, P. Farah, A. Popp, W. A. Wall, A monolithic, mortar-based interface coupling and solution scheme for finite element simulations of lithium-ion cells, International Journal for Numerical Methods in Engineering 114 (13) (2018) 1411–1437.

[52] R. Fang, M. Kronbichler, M. Wurzer, W. A. Wall, Parallel, physics-oriented, monolithic solvers for three-dimensional, coupled finite element models of lithium-ion cells, Computer Methods in Applied Mechanics and Engineering 350 (2019) 803–835.

[53] F. Verdugo, W. A. Wall, Unified computational framework for the efficient solution of n-field coupled problems with monolithic schemes, Computer Methods in Applied Mechanics and Engineering 310 (2016) 335–366.

[54] Y. Saad, M. H. Schultz, GMRES: A Generalized Minimal Residual Algorithm for Solving Nonsymmetric Linear Systems, SIAM Journal on Scientific and Statistical Computing 7 (3) (1986) 856–869.

[55] BACI: A Comprehensive Multi-Physics Simulation Framework, accessed: June 20, 2021. URL https://baci.pages.gitlab.lrz.de/website/

[56] U. Ayachit, The ParaView Guide: A Parallel Visualization Application, Kitware, Inc., USA, 2015.

[57] The MathWorks, Inc., MATLAB R2017b (9.3.0.713579) (2017).

[58] G. M. Goldin, A. M. Colclasure, A. H. Wiedemann, R. J. Kee, Three-dimensional particle-resolved models of Li-ion batteries to assist the evaluation of empirical parameters in one-dimensional models, Electrochimica Acta 64 (2012) 118–129.

[59] Computational Simulation Software, LLC, Trelis Pro 15.2.2 (64 bit) (2016).

[60] M. Ebner, F. Geldmacher, F. Marone, M. Stampanoni, V. Wood, X-Ray Tomography of Porous, Transition Metal Oxide Based Lithium Ion Battery Electrodes, Advanced Energy Materials 3 (7) (2013) 845–850.

[61] Materialise NV, Mimics 16.0 for X64, Platform V16.0.0.235 (2013).

[62] Materialise NV, 3-matic, Base, V8.0.0.113 (2013).

[63] C. Geuzaine, J.-F. Remacle, Gmsh: A 3-D finite element mesh generator with built-in pre- and post-processing facilities, International Journal for Numerical Methods in Engineering 79 (11) (2009) 1309–1331.

[64] B. V. Ratnakumar, M. C. Smart, Lithium Plating Behavior in Lithium-ion Cells, ECS Transactions 25 (36) (2010) 241–252.

[65] S. Schindler, M. Bauer, M. Petzl, M. A. Danzer, Voltage relaxation and impedance spectroscopy as in-operando methods for the detection of lithium plating on graphitic anodes in commercial lithium-ion cells, Journal of Power Sources 304 (2016) 170–180.

[66] J.-P. Jones, M. C. Smart, F. C. Krause, R. V. Bugga, The Effect of Electrolyte Additives upon Lithium Plating during Low Temperature Charging of Graphite-LiNiCoAlO$_2$ Lithium-Ion Three Electrode Cells, Journal of The Electrochemical Society 167 (2) (2020) 020536.

[67] S. Hein, A. Latz, Lithium Plating and Stripping in the Framework of a 3D Electrochemical Model, ECS Transactions 69 (1) (2015) 3–5.

[68] F. Single, B. Horstmann, A. Latz, Dynamics and morphology of solid electrolyte interphase (SEI), Physical Chemistry Chemical Physics 18 (2016) 17810–17814.

[69] F. Single, A. Latz, B. Horstmann, Identifying the Mechanism of Continued Growth of the Solid–Electrolyte Interphase, ChemSusChem 11 (12) (2018) 1950–1955.

[70] D. Juarez-Robles, A. A. Vyas, C. Fear, J. A. Jeevarajan, P. P. Mukherjee, Overcharge and Aging Analytics of Li-Ion Cells, Journal of The Electrochemical Society 167 (9) (2020) 090547.

[71] D. Juarez-Robles, A. A. Vyas, C. Fear, J. A. Jeevarajan, P. P. Mukherjee, Overdischarge and Aging Analytics of Li-Ion Cells, Journal of The Electrochemical Society 167 (9) (2020) 090558.

[72] J. Lück, A. Latz, Theory of reactions at electrified interfaces, Physical Chemistry Chemical Physics 18 (2016) 17799–17804.

[73] J. Lück, A. Latz, Modeling of the electrochemical double layer and its impact on intercalation reactions, Physical Chemistry Chemical Physics 20 (2018) 27804–27821.

[74] Z. Chen, Y. Qin, K. Amine, Redox shuttles for safer lithium-ion batteries, Electrochimica Acta 54 (24) (2009) 5605–5613.

[75] T. R. Jow, M. B. Marx, J. L. Allen, Distinguishing Li^+ Charge Transfer Kinetics at NCA/Electrolyte and Graphite/Electrolyte Interfaces, and NCA/Electrolyte and LFP/Electrolyte Interfaces in Li-Ion Cells, Journal of The Electrochemical Society 159 (5) (2012) A604–A612.

[76] J. Langer, V. Epp, P. Heitjans, F. A. Mautner, M. Wilkening, Lithium motion in the anode material LiC_6 as seen via time-domain ^7Li NMR, Physical Review B 88 (2013) 094304.

Declaration of interests

☒ The authors declare that they have no known competing financial interests or personal relationships that could have appeared to influence the work reported in this paper.

☐The authors declare the following financial interests/personal relationships which may be considered as potential competing interests: